A FAMILY OF SCHEMES FOR KINEMATIC FLOWS WITH DISCONTINUOUS FLUX

R. BÜRGER[A], A. GARCÍA[A], K.H. KARLSEN[B], AND J.D. TOWERS[C]

ABSTRACT. Multiphase flows of suspensions and emulsions are frequently approximated by spatially one-dimensional kinematic models, in which the velocity of each species of the disperse phase is an explicitly given function of the vector of concentrations of all species. The continuity equations for all species then form a system of conservation laws which describes spatial segregation and the creation of areas of different composition. This class of models also includes multi-class traffic flow, where vehicles belong to different classes according to their preferential velocities. Recently, these models were extended to fluxes that depend discontinuously on the spatial coordinate, which appear in clarifier-thickener models, in duct flows with abruptly varying cross-sectional area, and in traffic flow with variable road surface conditions.

This paper presents a new family of numerical schemes for such kinematic flows with a discontinuous flux. It is shown how a very simple scheme for the scalar case, which is adapted to the "concentration times velocity" structure of the flux, can be extended to kinematic models with phase velocities that change sign, flows with two or more species (the system case), and discontinuous fluxes. In addition, a MUSCL-type upgrade in combination with a Runge-Kutta type time discretization can be devised to attain second-order accuracy. It is proved that system variants of the scheme preserve an invariant region of admissible concentration vectors, provided that all velocities have the same sign. Moreover, for the relevant case of a multiplicative flux discontinuity, it is proved that scalar versions converge to a BV_t entropy solution of the model. In the latter case, the compactness proof involves a novel uniform but local estimate of the spatial total variation of the approximate solutions.

Numerical examples illustrate the performance of all variants within the new family of schemes applied to abstract examples and problems of sedimentation, traffic flow, and the settling of oil-in-water emulsions.

1. INTRODUCTION

1.1. **Scope of the paper.** Numerous multiphase flows involve the flow of one disperse substance, for example solid mineral particles or oil droplets in an emulsion, through a continuous phase, say a liquid or gas. In many cases, the disperse substance consists of small particles that belong to different species which differ in some characteristic quantity such as size or density. The different species will segregate and create areas of different composition, which is the most interesting property in many applications. Similar models also includes certain continuum approximations of traffic flow of vehicles on a highway if cars with drivers having different preferential velocities are identified as different species.

In general, we distinguish between N different species that give rise to N superimposed continuous phases associated with volume fractions (or densities) $\phi_1, \ldots, \phi_N$. If v_i is the one-dimensional velocity of species i, then the continuity equations of the N species in differential form are

$$\partial_t \phi_i + \partial_x(\phi_i v_i) = 0, \quad i = 1, \ldots, N, \tag{1.1}$$

where t is time and x is the spatial position. The basic assumption of kinematic models is that the velocities $v_1, \ldots, v_N$ are given functions of the vector $\Phi := (\phi_1, \ldots, \phi_N)^{\mathrm{T}}$ of local concentrations of all species, $v_i = v_i(\Phi)$. This yields systems of conservation laws of the type

$$\partial_t \phi_i + \partial_x(\phi_i v_i(\Phi)) = 0, \quad i = 1, \ldots, N. \tag{1.2}$$

We focus on three specific kinematic models that recently attracted interest: one of multi-species traffic flow [1, 2, 3, 4, 5, 6], one of sedimentation of polydisperse suspensions [7, 8, 9, 10, 11], and one of separation of oil-in-water dispersions [12].

All these applications also give rise to spatially non-homogeneous flows, in which the velocity v_i not only depends on Φ, but also on a vector of parameters $\boldsymbol{\gamma}_i$ that is a function of the spatial position x, $\boldsymbol{\gamma}_i = \boldsymbol{\gamma}_i(x)$. While models for which $\boldsymbol{\gamma}_i$ depends, for example, Lipschitz continuously on x lead to conservation laws that can be treated with standard analytical and numerical methods, we are here interested in the case that $\boldsymbol{\gamma}_i$ depends discontinuously on x; more precisely, we assume that $\boldsymbol{\gamma}_i$ is piecewise smooth with a finite number of discontinuities. The vector $\boldsymbol{\gamma}_i(x)$ may describe, for instance, abruptly changing road surface conditions in the traffic flow model, as was done in [13, 14] for a single-species model; singular feed sources and diverging bulk flows in clarifier-thickener models [15, 16]; and abruptly changing cross-sectional areas in vessels for the settling of suspensions and emulsions.

It is the purpose of this contribution to formulate, in part analyze, and present numerical experiments for easy-to-implement numerical schemes for kinematic models, in which the numerical flux is explicitly based on the "concentration times velocity" structure of each flux component. The starting point is a simple two-point monotone numerical flux for scalar ($N = 1$) kinematic flows with a non-negative velocity function $v = v(\phi)$. We develop extensions of the scheme defined by this numerical flux to equations with a velocity of variable sign, to equations with a discontinuous, to systems of conservation laws ($N \geq 2$ species), and finally to schemes with second-order accuracy. All these variants form the family of new schemes under study. It is proved that for $N \geq 1$ flows with non-negative velocities, the schemes preserve an invariant region, i.e. generate approximations that assume values in the domain of physically relevant concentrations only. For the scalar case ($N = 1$) and a discontinuous flux, we prove convergence to a BV_t entropy solution. The proof is based on a new uniform but local estimate of the spatial total variation of approximate solutions. Numerical experiments demonstrate the performance of the new family of schemes.

What is intriguing about the new schemes is that (other than an estimate of the spectral radius for the CFL condition) they do not require any calculation of eigenvalues, eigenvectors, field-by-field decomposition, flux vector splitting etc. that are usually required for an upwind scheme. In this sense they are like a central scheme. However, in many cases the first-order accurate version of the new schemes is much less dissipative than the first-order version of the central scheme (the Lax-Friedrichs scheme).

1.2. Multi-species kinematic models.

In this and the following section, we recall some known properties and discretizations of kinematic models of the type (1.2), while some results related to conservation laws with discontinuous flux are reviewed in Section 1.4.

In many applications, the number N of species may be large, and the different species in these applications are competitive. It is therefore convenient to assume a maximal density $\phi_{\max}$ (for example, a maximal 'bumper-to-bumper' car density in traffic models or the maximal sphere packing density $\phi_{\max} \approx 0.66$ in sedimentation models), such that the phase space for (1.2) is

$$(1.3) \qquad \mathcal{D}_{\phi_{\max}} := \big\{ \Phi = (\phi_1, \dots, \phi_N)^{\mathrm{T}} \in \mathbb{R}^N : \ \phi_1 \geq 0, \dots, \phi_N \geq 0, \ \phi := \phi_1 + \dots + \phi_N \leq \phi_{\max} \big\}.$$

Introducing the flux vector

$$(1.4) \qquad \mathbf{f}(\Phi) = \big(f_1(\Phi), \dots, f_N(\Phi) \big)^{\mathrm{T}} := \big(\phi_1 v_1(\Phi), \dots, \phi_N v_N(\Phi) \big)^{\mathrm{T}},$$

we can rewrite (1.2) as the nonlinear system of conservation laws

$$(1.5) \qquad \partial_t \Phi + \partial_x \mathbf{f}(\Phi) = 0.$$

It is well known that solutions of (1.5) are discontinuous in general, and that the propagation speed $\sigma(\Phi^+, \Phi^-)$ of a discontinuity in the concentration field ϕ_i separating the states Φ^+ and Φ^- is given by the Rankine-Hugoniot condition

$$\sigma = \frac{f_i(\Phi^+) - f_i(\Phi^-)}{\phi_i^+ - \phi_i^-}.$$

We recall that the system (1.5) is called *hyperbolic* at a state Φ if the Jacobian $\mathcal{J}_{\mathbf{f}}(\Phi) := (\partial f_i / \partial \phi_k)_{1 \le i,k \le N}$ only has real eigenvalues, and *strictly hyperbolic* if these are moreover pairwise distinct.

The kinematic traffic model for $N = 1$ goes back to Lighthill and Whitham [17] and Richards [18] ("LWR model"); for the sedimentation of suspensions, the classic reference is Kynch [19]. The extension of the LWR model to multi-class traffic flow was proposed by Benzoni-Gavage and Colombo [1] and Wong and Wong [2], while extensions of the sedimentation model to several species have been suggested for several decades (see [11, 20] for reviews), mainly in the chemical engineering literature. The application of available tools of mathematical and numerical analysis to kinematic flow models is difficult due to the dependence of the functions $v_i(\Phi)$ on all variables $\phi_1, \ldots, \phi_N$, which in general is nonlinear. Closed formulas for the eigenvalues and eigenvectors of $\mathcal{J}_{\mathbf{f}}(\Phi)$ are at least complicated, if not unavailable for $N \ge 5$. It is therefore in general not possible to solve the Riemann problem for (1.2) in closed form. Moreover, for multi-species kinematic models eigenvalues lack a direct physical interpretation, and in particular do not coincide with any of the phase velocities $v_1, \ldots, v_N$.

Advances were made recently in the hyperbolicity analysis and characterization of eigenvalues of kinematic models. For the model of settling of oil-in-water dispersions, Rosso and Sona [12] proved for arbitrary N strict hyperbolicity in $\mathcal{D}_{\phi_{\max}}$. The proof is based on deriving an explicit closed formula of the characteristic polynomial of $\mathcal{J}_{\mathbf{f}}(\Phi)$, and discussing its zeros. Berres et al. [7] proved in a similar way that the model [7, 21, 22] for the sedimentation of polydisperse suspensions utilized herein is strictly hyperbolic for arbitrary N, provided that all particles have the same density. The basic idea was also used by Zhang et al. [5] to prove strict hyperbolicity of the multi-class traffic model proposed in [1, 2].

1.3. **Numerical schemes for kinematic models.** Despite the new hyperbolicity results, insight into any specific N-species kinematic model with $N \ge 3$ can realistically be gained through numerical simulation only. High resolution schemes for systems of conservation laws, which approximate discontinuities sharply and without spurious oscillations and are at least second-order accurate in smooth regions, are natural candidates for the numerical solution of (1.2). For example, Wong, Shu and their collaborators [4, 6] applied weighted essentially non-oscillatory (WENO) schemes to the traffic model, while the first and third authors and collaborators [7, 20, 23, 24] employed central difference schemes [25, 26] for the sedimentation model. Meanwhile, central schemes have also been applied to a number of real-world problems of polydisperse sedimentation, see for example Xue and Sun [10], Simura and Ozawa [27] and Wang et al. [28]. Recently [29], WENO schemes were combined with a multiresolution technique to yield a numerical method for kinematic models that adaptively concentrates computational effort on zones of strong variation.

All these methods are based on schemes that can be applied universally to systems of conservation laws, and that are not tailored to a particular algebraic structure of the flux vector. Our new family of schemes does, however, explicitly make use of the structure of fluxes for kinematic models. The schemes, which are first-order accurate, can be upgraded to higher order accuracy by employing MUSCL-type techniques.

1.4. **Well-posedness analysis and numerical schemes for conservation laws with discontinuous flux.** To put the treatment in the proper perspective, let us first recall some known results for the equation $u_t + f(\boldsymbol{\gamma}(x), u)_x = 0$. The basic difficulty is that its well-posedness is not a straightforward limit case of the standard theory for conservation laws with a flux that depends smoothly on x. In fact, several extensions of the Kružkov entropy solution concept [30] to conservation laws with a discontinuous flux were proposed in recent years [31, 32, 33, 34, 35, 36, 37, 38, 39, 40, 41, 42, 43, 44, 45]. Each of these concepts is supported by a convergence analysis of a numerical scheme; the differences between them appear in the respective admissibility conditions for stationary jumps of the solution across the discontinuities of $\boldsymbol{\gamma}$ [46].

The choice of the entropy solution concept depends on the regularizing viscous physical model. For clarifier-thickener models, the appropriate concept emerges from the limit $\varepsilon \to 0$ of a viscous regularization εu_{xx} with a diffusion constant $\varepsilon > 0$ [47]. Diehl advanced thorough analyses and construction of exact entropy solutions for clarifier-thickener models, which are culminating in his series of papers "Operating charts for continuous sedimentation" [48, 49, 50, 51]. On the other hand, the authors with collaborators made a series of contributions (including [15, 16, 47, 52]) to the well-posedness and numerical analysis for these models, whose basic non-standard ingredient is a singular feed source that produces diverging bulk

flows, which causes the discontinuous x-dependence of the flux. The same entropy solution concept has also been applied to establish well-posedness, and to construct a working numerical scheme, for a model of single-species traffic flow with abruptly changing road surface conditions [14].

The rigorous analysis is limited to the scalar case, but the numerical schemes that have been used to constructively establish existence of weak solutions to the scalar clarifier-thickener model also possess working versions for systems with discontinuous flux. In the context of clarifier-thickener models, such systems model fluidization and classification units for polydisperse suspensions, see [53, 54].

1.5. **Contents of the paper.** The remainder of the paper is organized as follows. In Section 2, three specific kinematic models are presented. Section 2.1 presents the multi-class kinematic traffic model, which gives rise to an initial-value problem with periodic boundary conditions. Next, in Section 2.2, we outline the polydisperse sedimentation model, for which the zero-flux boundary condition is relevant. A similar model for the separation of oil-in-water dispersions is mentioned in Section 2.3. The distinctive property of the sedimentation model is that the phase velocities of the particle species may be positive, zero or negative, due to buoyancy effects, while in the two other models, these velocities are always non-negative.

Section 3 is devoted to the presentation of the family of schemes. To this end, we first introduce in Section 3.1 the basic time and space discretizations. In Section 3.2, the scalar versions (i.e., for $N = 1$) of the schemes are introduced, starting with Schemes 1 and 2 for fluxes with non-negative velocity and a velocity of variable sign, respectively. It is shown that both schemes are monotone provided that a CFL condition is satisfied. Furthermore, we extend Scheme 1 to an equation with discontinuous flux (Scheme 3). In Section 3.3, we formulate schemes for multi-species kinematic models, that is, for systems of conservation laws ($N \geq 1$). The systems variants of the scalar Schemes 1 and 3 for models with non-negative velocities only are Schemes 4 and 5. For models with velocities of variable sign, the direct extension of the scalar Scheme 2 is Scheme 6. However, as is detailed in Section 3.3, this scheme produces sharply resolved interfaces, but overshoots in certain situations. An analysis of the viscosity coefficients of Scheme 6 leads to the improved Scheme 7. It turns out that for the sedimentation model, this scheme still produces overshoots near stationary discontinuities; for this reason, the final scheme advocated for systems with velocities of variable sign is Scheme 8, which is slightly more viscous than Scheme 7. One desirable property of schemes for kinematic models consists in the preservation of an invariant region, i.e. under a suitable CFL condition, the scheme should produce approximations that assume values within the physically relevant phase space only (i.e., concentrations should be non-negative and sum up at most to the maximal concentration). We show in Section 3.4 that Scheme 5, applied to the traffic model, and Scheme 4, applied to the oil-in-water dispersion model, indeed do have these properties. Experience with the traffic and oil-in-water dispersion model leads us to propose a working CFL condition also for the sedimentation model. In Section 3.5 we demonstrate how the schemes developed so far can be improved to second-order accuracy both in space and time by combining Runge-Kutta temporal differencing with MUSCL-type spatial differencing. The latter involves the use of slope limiter functions; we refer to the variants with the minmod and Van Leer limiter functions as Scheme 9 and 10, respectively. We show that if applied to scalar problems with a flux that does not depend on x, these schemes preserve the maximum principle and the TVD property of the first-order version under the same CFL condition.

In Section 4, we consider a scalar initial-boundary value problem with periodic boundary conditions and a discontinuous flux, and prove that Scheme 3 generates a sequence of approximate solutions that converge to the unique BV_t entropy solution of the problem as the mesh parameters tend to zero. One basic ingredient of the compactness argument involved here is a new type of local but uniform estimate of the total spatial variation of approximate solutions. This type of argument (see Lemma 4.2 in Section 4 and its proof) is new, and has not been used in any previous work on discontinuous flux problems.

In Section 5, we present eight numerical examples to demonstrate the performance of the schemes of the family, especially compared to variants of the Lax-Friedrichs scheme. Examples 1 and 2 refer to "abstract" scalar equations. Example 3 presents a simulation of a scalar clarifier-thickener model, and allows comparison with a numerical result published in [16]. In Example 4, we study the multi-species traffic model with $N = 9$, but without flux discontinuities, and choose parameters in such a way that results can be compared with

those presented in [4]. In addition, for this example (and for Example 6) we present a history of approximate L^1 numerical errors. This is done for the first- and second-order variants of the scheme, as well as for the corresponding variants of the LxF scheme. Example 5 corresponds to the traffic model with a discontinuously varying parameter, and the numerical results can be compared those of Zhang et al. [6]. In Example 6, we simulate the settling of a suspension with $N = 2$ species in a column using parameters from a well-documented experiment by Schneider et al. [55]. These results, as those of Example 7, where we consider a suspension with $N = 11$ species, can also be compared with those of [29]. Finally, Example 8 presents a simulation of the settling of an oil-in-water dispersion with $N = 10$ species.

2. Examples of kinematic flow models

2.1. **Traffic flow models.** The classical LWR kinematic wave model [17, 18] for unidirectional traffic flow on a single-lane highway starts from the principle of "conservation of cars", where ϕ is the density of cars as a function of distance x and time t and $v = v(x, t)$ is the velocity of the car located at position x at time t:

$$(2.1) \qquad \partial_t \phi + \partial_x (\phi v) = 0, \quad x \in \mathbb{R}, \quad t > 0,$$

The original LWR model (2.1) is a single-species model ($N = 1$), whose basic assumption $v = v(\phi)$ states that each driver instantaneously adjusts his velocity to the local car density. A common choice is $v(\phi) = v_{\max} V(\phi)$, where $v_{\max}$ is a preferential velocity a assumed on a free highway, and $V(\phi)$ is a hindrance function taking into account that the presence of other cars urges each driver to adjust his speed. Thus, the flux is

$$(2.2) \qquad f(\phi) := \phi v(\phi) = \begin{cases} v_{\max} \phi V(\phi/\phi_{\max}) & \text{for } 0 \le \phi \le \phi_{\max}, \\ 0 & \text{otherwise}, \end{cases}$$

where $\phi_{\max}$ is the maximum "bumper-to-bumper" car density.

Recently, Benzoni-Gavage and Colombo [1] and Wong and Wong [2] independently formulated an extension of the LWR model to multi-class traffic flow, considering that cars belong to a finite number N of classes (species), each associated with a function $v = v_i(\Phi)$. It is assumed that drivers of each species adjust their velocity to the global car density $\phi = \phi_1 + \cdots + \phi_N$ seen at a point (x, t), which means that $v_i(\Phi(x, t)) = v_i(\phi(x, t))$ for $i = 1, \ldots, N$, and that all drivers adjust their velocity in the same way, such that

$$(2.3) \qquad v_i(\Phi) = v_{\max}^i V(\phi/\phi_{\max}), \quad i = 1, \ldots, N.$$

Here, $v_{\max}^i$ is the preferential (maximum) of species i and the function $V : [0, \phi_{\max}] \to [0, 1]$ describes the attitude of drivers [1], that is, represents the same hindrance function as in the single-class case.

Also of interest are models where we replace (2.3) by

$$(2.4) \qquad v_i = v_i(x, \Phi) = v_{\max}^i(x) V(\phi/\phi_{\max}(x)), \quad v_{\max}^i(x) > 0, \quad i = 1, \ldots, N.$$

By allowing v_i to vary spatially through the coefficients $v_{\max}^i(x)$ and $\phi_{\max}(x)$, it is possible to model road conditions that change from location to location.

For the traffic model, we assume a circular road of length L and assume an initial traffic density

$$(2.5) \qquad \Phi(x, 0) = \Phi^0(x) = \left(\phi_1^0(x), \ldots, \phi_N^0(x) \right)^{\mathrm{T}} \in \mathcal{D}_{\phi_{\max}}, \quad 0 \le x \le L.$$

The periodicity condition is

$$\phi_i(0, t) = \phi_i(L, t), \quad t > 0, \quad i = 1, \ldots, N;$$

however, we only consider compactly supported data and relatively short simulation times (shorter than necessary for completing a loop), so that our solutions are also solutions to the initial-value problem posed for $x \in \mathbb{R}$, that is, for an infinite road.

2.2. **Sedimentation of polydisperse suspensions.** We consider a polydisperse suspension of rigid spherical particles which are dispersed in a viscous fluid of density ϱ_{f} and of dynamic viscosity μ_{f}. The solid particles belong to N different species having sizes (diameters) $d_1 \geq d_2 \geq \cdots \geq d_N$ and densities $\varrho_1, \ldots, \varrho_N$, where $d_i \neq d_j$ or $\varrho_i \neq \varrho_j$ for $i \neq j$. Model equations for the three-dimensional motion of such a mixture were derived in [8], based on earlier work by Masliyah [22] and Lockett and Bassoon [21]. We consider here the kinematic model obtained by reducing these equations to one space dimension, see [8] for details. The relevant parameters are $\delta_i := d_i^2/d_1^2$ and $\bar{\varrho}_i := \varrho_i - \varrho_{\mathrm{f}}$ for $i = 1, \ldots, N$. Here, $\phi_{\max}$ denotes a maximum solids volume fraction, which we here assume to be constant. Moreover, we introduce the vector $\bar{\varrho} := (\bar{\varrho}_1, \ldots, \bar{\varrho}_N)^{\mathrm{T}}$, the cumulative solids fraction $\phi := \phi_1 + \cdots + \phi_N$, the viscosity parameter $\mu := gd_1^2/(18\mu_{\mathrm{f}}) > 0$, where g is the acceleration of gravity, and the hindered settling factor $V = V(\phi)$, which may be chosen as

$$(2.6) \qquad V(\phi) = \begin{cases} (1-\phi)^{n-2} & \text{if } \Phi \in \mathcal{D}_{\phi_{\max}}, \\ 0 & \text{otherwise,} \end{cases} \quad n > 2.$$

The phase velocity of particle species i is then given by

$$(2.7) \qquad v_i(\Phi) = \mu V(\phi) \left[\delta_i(\bar{\varrho}_i - \bar{\varrho}^{\mathrm{T}}\Phi) - \sum_{m=1}^N \delta_m \phi_m (\bar{\varrho}_m - \bar{\varrho}^{\mathrm{T}}\Phi) \right], \quad i = 1, \ldots, N.$$

For one-dimensional batch settling of a suspension in a closed vessel of depth L, the initial condition is again (2.5), while the zero-flux boundary conditions are

$$(2.8) \qquad \mathbf{f}|_{x=0} = \mathbf{f}|_{x=L} = 0.$$

If the particles differ in size only (i.e., $\varrho_1 = \varrho_2 = \cdots = \varrho_N =: \varrho_{\mathrm{s}}$), then (2.7) simplifies to the following expression, where $v_\infty = \mu(\varrho_{\mathrm{s}} - \varrho_{\mathrm{f}})$ is the settling velocity of a single particle of the largest species in an unbounded medium (the so-called Stokes velocity of the largest species):

$$(2.9) \qquad v_i(\Phi) = v_\infty(1-\phi)V(\phi)\big(\delta_i - (\delta_1\phi_1 + \cdots + \delta_N\phi_N)\big), \quad i = 1, \ldots, N.$$

In [7] it is proved that for equal-density particles ($\bar{\varrho} = \cdots = \bar{\varrho}_N = \varrho_{\mathrm{s}} - \varrho_{\mathrm{f}}$), *arbitrary* N and particle size distributions, the system (1.5) is strictly hyperbolic for all $\Phi \in \mathcal{D}$ with $\phi_1 > 0, \ldots, \phi_N > 0$ and $\phi < 1$ if the flux vector (2.7) is chosen. As mentioned in Section 1.2, the proof proceeds in a similar fashion to that of Rosso and Sona [12] outlined in Section 1.2.

2.3. **Separation of oil-in-water dispersions.** Kinematic models have also been proposed for the sedimentation of small oil droplets in liquid-liquid dispersions. The separation process is similar to the settling of a polydisperse suspension, the major difference being that since the density of oil is smaller than that of water, the oil droplets move upwards, a process called *creaming*; however, to make results comparable with the sedimentation model, we assume that the separation takes place in the direction of the positive x-axis, so x is considered here to be a height variable. Numerous contributions to kinematic models for liquid-liquid dispersions have been made by Hartland, Jeelani, and their collaborators, see for example [56, 57, 58, 59, 60]. The analogy between suspension and dispersion models is also emphasized by Nadiv et al. [61] and Frising et al. [62]. The model utilized herein is due to Rosso and Sona [12], who consider the separation of small oil droplets in an oil-in-water dispersion. (It is worth mentioning that Rosso and Sona explicitly refer to [63], a doctoral thesis prepared under Hartland's guidance.)

The model outlined in [12] can be written in the form (1.2) if we consider oil droplets of N different volumes $\mathcal{V}_\infty > \mathcal{V}_2 > \cdots > \mathcal{V}_N > 0$, where x is the upward-increasing height variable and $\phi_i = \phi_i(x, t)$ is the volume fraction occupied by droplets of volume $\mathcal{V}_i$. The model is similar to that of sedimentation, but as the authors argue, the differential motion of the particle species is not driven by the dispersion-water density difference, which actually can be considered constant, but rather by differences in viscosity. The basic nonlinearity is introduced by a viscosity function $\mu_{\mathrm{d}} = \mu_{\mathrm{d}}(\Phi) = \mu_{\mathrm{d}}(\phi_1, \ldots, \phi_N)$. If we denote again by μ_{f} the viscosity of pure water (without oil), then $\mu_{\mathrm{d}}(\Phi)$ is assumed to satisfy

$$\mu_{\mathrm{d}} \in C^1(\mathcal{D}); \quad \mu_{\mathrm{d}}(\Phi) > 0, \quad \frac{\partial \mu_{\mathrm{d}}}{\partial \phi_1} > 0, \ldots, \frac{\partial \mu_{\mathrm{d}}}{\partial \phi_N} > 0 \quad \forall \Phi \in \mathcal{D}; \quad \mu_{\mathrm{d}}(0, \ldots, 0) = \mu_{\mathrm{f}}.$$

The velocity functions $v_1(\Phi), \ldots, v_N(\Phi)$ are then given by

$$(2.10) \qquad v_i(\Phi) = c\frac{\mathcal{V}_i^{2/3}}{\mu_{\mathrm{d}}(\Phi)}(1-\phi), \quad i = 1, \ldots, N, \quad c := \frac{2g(\varrho_{\mathrm{f}} - \varrho_{\mathrm{oil}})}{9(4\pi/3)^{2/3}},$$

where g, ϱ_{f} and ϱ_{oil} denote the acceleration of gravity, the density of pure water and density of pure oil, respectively. For separation of a dispersion in a column of height L, we may again employ the initial and boundary conditions (2.5) and (2.8).

3. Numerical schemes

Section 2 shows that we are interested in schemes for kinematic models with a flux that possibly depends discontinuously on the spatial position x. Thus, seek weak solutions to the initial value problem

$$(3.1) \qquad \begin{aligned} \partial_t \phi_i + \partial_x f_i(x, \Phi) &= 0, \quad (x, t) \in (0, L) \times (0, T) =: \Pi_T, \quad i = 1, \ldots, N, \\ f_i(x, \Phi) &= \phi_i v_i\big(\boldsymbol{\gamma}_i(x), \Phi\big), \quad \Phi(x, 0) = \Phi^0(x), \quad x \in (0, L), \end{aligned}$$

which may be supplemented by periodic boundary conditions

$$\Phi(0, t) = \Phi(L, t), \quad t > 0,$$

or zero-flux boundary conditions

$$f_i(0, \Phi) = f_i(L, \Phi) = 0, \quad i = 1, \ldots, N.$$

This setup is general enough to include the models discussed in the previous section.

3.1. **Discretizations.** We start by discretizing the domain $[0, L] \times [0, T]$. To discretize the spatial interval $[0, L]$, we choose a mesh width Δx and an integer $\mathcal{J}$ such that $(\mathcal{J} + 1)\Delta x = L$, and set

$$x_j = (j + 1/2)\Delta x, \quad j = -1/2, 0, 1/2, 1, 3/2, \ldots, \mathcal{J} - 1, \mathcal{J} + 1/2.$$

With this setup, $x_{-1/2} = 0$, $x_{\mathcal{J}+1/2} = L$. We discretize the time interval $[0, T]$ by selecting an integer $\mathcal{N}$ and a sequence of temporal mesh widths Δt_n, and defining $t_0 := 0$ and $t_{n+1} := t_n + \Delta t_n$ for $n = 0, 1, \ldots, \mathcal{N}$ subject to the condition $\Delta t_0 + \cdots + \Delta t_{\mathcal{N}-1} = T$. The ratio $\lambda_n := \Delta t_n / \Delta x$ is always assumed to satisfy a CFL condition, which will be specified below. Our numerical schemes will generate an approximation $\Phi_j^n \approx \Phi(x_j, t_n)$ defined at the mesh points (x_j, t_n) for $j \in \{0, 1, \ldots, \mathcal{J}\} =: \mathbb{Z}_{\mathcal{J}}$ and $n = 0, 1, \ldots, \mathcal{N}$. For our first-order accurate scheme, we start by discretizing the initial data and the parameter vectors

$$\Phi_j^0 = \Phi_0\big(x_j^+\big) := \lim_{x \downarrow x_j} \Phi_0(x), \quad \boldsymbol{\gamma}_{i,j} := \boldsymbol{\gamma}_i\big(x_j^+\big), \quad i = 1, \ldots, N.$$

Here we have arbitrarily chosen the limit from above to resolve the ambiguities at possible jump discontinuities in the data. This is somewhat arbitrary; we could also use the limit from below, or any average of the two. We then march the solution forward in time according to

$$(3.2) \qquad \Phi_j^{n+1} = \Phi_j^n - \lambda_n\big(\boldsymbol{h}_{j+1/2}^n - \boldsymbol{h}_{j-1/2}^n\big), \quad j \in \mathbb{Z}_{\mathcal{J}}, \quad n = 0, 1, \ldots, \mathcal{N}.$$

The numerical flux vector $\boldsymbol{h}_{j+1/2}^n$ is

$$(3.3) \qquad \boldsymbol{h}_{j+1/2}^n = \big(h_1\big(\boldsymbol{\gamma}_{1,j+1}, \Phi_{j+1}^n, \Phi_j^n\big), \ldots, h_N\big(\boldsymbol{\gamma}_{N,j+1}, \Phi_{j+1}^n, \Phi_j^n\big)\big)^{\mathrm{T}}.$$

Recall that we are considering two types of boundary conditions. When dealing with zero flux boundary conditions, we always set

$$(3.4) \qquad \boldsymbol{h}_{-1/2}^n = \boldsymbol{h}_{\mathcal{J}+1/2}^n = 0, \quad n = 0, 1, 2, \ldots$$

When dealing with periodic boundary conditions, we may have formulas where $j < -1/2$ or $j > \mathcal{J} + 1/2$. In such cases we simply interpret j modulo $(\mathcal{J} + 1)$, in such a way that it lies within the proper range. For periodic boundary conditions, we will always have

$$(3.5) \qquad \boldsymbol{h}_{-1/2}^n = \boldsymbol{h}_{\mathcal{J}+1/2}^n, \quad n = 0, \ldots, \mathcal{N}.$$

With these observations, we can deal with both types of boundary conditions simultaneously, and mostly avoid discussing special processing at the boundaries.

3.2. **The scalar case.** To discuss our new numerical flux in the simplest possible setting, we start with scalar kinematic wave models, where no spatially dependent parameter vector occurs:

$$(3.6) \qquad\qquad\qquad \phi_t + f(\phi)_x = 0,$$

where the flux takes the special form for kinematic flow models

$$(3.7) \qquad\qquad\qquad f(\phi) = \phi v(\phi).$$

The assumptions are that $\phi \geq 0$, and that $v(\phi)$ is given by a positive default velocity multiplying a hindrance function. Since the hindrance increases with ϕ, the assumptions $v(\phi) \geq 0$ and $v'(\phi) \leq 0$ are very natural, and clearly satisfied for all examples of kinematic models considered herein. For traffic flow, ϕ is the traffic density, and v is the velocity of cars as a function of density, while for sedimentation, ϕ is the solids volume fraction and v is the solids phase velocity.

3.2.1. *Scheme 1 for scalar equations ($N = 1$) with non-negative velocity.* The following is a two-point numerical flux consistent with the actual flux (3.7):

$$(3.8) \qquad\qquad\qquad h(\phi_{j+1}, \phi_j) := \phi_j v(\phi_{j+1}).$$

For easy reference, we refer to the scheme (3.2), (3.3) with $N = 1$, $\boldsymbol{\gamma} \equiv$ const. and the flux (3.8) as Scheme 1. Due to the special structure of this problem ($\phi \geq 0$, $v(\phi) \geq 0$, $v'(\phi) \leq 0$), Scheme 1 is monotone [64], meaning that the function $h(\phi_{j+1}, \phi_j)$ is non-increasing with respect to ϕ_{j+1} and nondecreasing with respect to ϕ_j. Therefore, Scheme 1 produces approximations that converge to the correct entropy solution to the conservation law (3.6). However, these approximations will be at best first order accurate. What makes the flux (3.8) interesting is that like the Lax-Friedrichs numerical flux, it is very simple (there is no Riemann solver involved), but in many cases it is less dissipative than the Lax-Friedrichs numerical flux. This motivates us to use (3.8), and various extensions to deal with systems and discontinuous coefficients, as a starting point to build a second-order scheme.

3.2.2. *Scheme 2 for scalar equations ($N = 1$) with a velocity of variable sign.* Motivated by the polydisperse settling model, where the velocities may become negative, we next consider the scalar case where the velocity v may become negative. It is easy to check that the following modification of (3.8) is a flux that retains the monotonicity property in this more general situation:

$$(3.9) \qquad\qquad h(\phi_{j+1}, \phi_j) = \phi_j \max\{0, v(\phi_{j+1})\} + \phi_{j+1} \min\{0, v(\phi_{j+1})\}.$$

We refer to the scheme (3.2), (3.3) for $N = 1$ and $\boldsymbol{\gamma} \equiv$ const. with the flux (3.9) as Scheme 2. Another formulation of (3.9) that will be useful in what follows is the so-called viscous form:

$$(3.10) \qquad\qquad h(\phi_{j+1}, \phi_j) = \frac{1}{2}\big(f(\phi_{j+1}) + f(\phi_j)\big) - \frac{1}{2\lambda}Q(\phi_{j+1}, \phi_j)(\phi_{j+1} - \phi_j),$$

where the numerical viscosity coefficient $Q(\phi_{j+1}, \phi_j)$ is defined by

$$(3.11) \qquad\qquad Q(\phi_{j+1}, \phi_j) := \lambda\big|v(\phi_{j+1})\big| + \lambda\phi_j \frac{v(\phi_j) - v(\phi_{j+1})}{\phi_{j+1} - \phi_j}.$$

To derive CFL conditions, let us concentrate for now on the case where the boundary conditions are periodic. If we write Scheme 2 in incremental form

$$\phi_j^{n+1} = \phi_j^n + C_{j+1/2}\Delta_+\phi_j^n - D_{j-1/2}\Delta_-\phi_j^n,$$

where we define the spatial difference operators $\Delta_- V_j := V_j - V_{j-1}$ and $\Delta_+ V_j := V_{j+1} - V_j$, the incremental coefficients are given by

$$(3.12) \qquad C_{j+1/2} = \lambda\phi_j \frac{v(\phi_j^n) - v(\phi_{j+1}^n)}{\phi_{j+1}^n - \phi_j^n} - \lambda\min\{0, v(\phi_{j+1}^n)\}, \quad D_{j+1/2} = \lambda\max\{0, v(\phi_{j+1}^n)\}.$$

To have a maximum principle

$$(3.13) \qquad\qquad \min\{\phi_{j-1}^n, \phi_j^n, \phi_{j+1}^n\} \leq \phi_j^{n+1} \leq \max\{\phi_{j-1}^n, \phi_j^n, \phi_{j+1}^n\}$$

and the Total Variation Decreasing (TVD) property

$$(3.14) \qquad \sum_{j=0}^{\mathcal{J}} \left| \phi_{j+1}^{n+1} - \phi_j^{n+1} \right| \leq \sum_{j=0}^{\mathcal{J}} \left| \phi_{j+1}^n - \phi_j^n \right|,$$

sufficient conditions are [65, 66]

$$C_{j+1/2} + D_{j+1/2} \leq 1, \quad C_{j+1/2} + D_{j-1/2} \leq 1, \quad C_{j+1/2} \geq 0, \quad D_{j+1/2} \geq 0.$$

It is clear from (3.12) that $C_{j+1/2} \geq 0$ and $D_{j+1/2} \geq 0$ are already satisfied. To enforce the first two inequalities, we impose the CFL conditions

$$(3.15) \qquad \lambda \max_{j \in \mathbb{Z}_{\mathcal{J}}} \left| v(\phi_j) \right| \leq \alpha, \quad \alpha = 1/4, \qquad \lambda \max_{j \in \mathbb{Z}_{\mathcal{J}}} \phi_j \cdot \max_{j \in \mathbb{Z}_{\mathcal{J}}} \left| v'(\phi_j) \right| \leq \alpha, \quad \alpha = 1/2.$$

In this paper we state a CFL condition, like those in (3.15), in terms of the number α for ease of comparison with other CFL conditions (with different values of α) that will appear elsewhere.

If the speed v is nonnegative, the second term on the right-hand side of the equation for $C_{j+1/2}$ in (3.12) is not present, and we can replace (3.15) by the less restrictive CFL conditions

$$(3.16) \qquad \lambda \max_{j \in \mathbb{Z}_{\mathcal{J}}} v(\phi_j) \leq \alpha, \quad \lambda \max_{j \in \mathbb{Z}_{\mathcal{J}}} \phi_j \cdot \max_{j \in \mathbb{Z}_{\mathcal{J}}} \left| v'(\phi_j) \right| \leq \alpha, \quad \alpha = 1/2.$$

3.2.3. *Scheme 3 for scalar equations ($N = 1$) with non-negative velocity with a discontinuous flux.* We will also consider scalar conservation laws of the form

$$(3.17) \qquad \phi_t + f\big(\boldsymbol{\gamma}(x), \phi\big)_x = 0, \quad f(\phi) = \phi v\big(\boldsymbol{\gamma}(x), \phi\big), \quad v(\boldsymbol{\gamma}, \phi) \geq 0,$$

where the spatially varying coefficient vector $\boldsymbol{\gamma}$ may have jump discontinuities. For the traffic flow model, the coefficient $\boldsymbol{\gamma}$ modulates the velocity function, and provides a way to model spatially varying road conditions. For the conservation law (3.17), our numerical flux becomes

$$(3.18) \qquad h(\boldsymbol{\gamma}_{j+1}, \phi_{j+1}, \phi_j) = \phi_j v(\boldsymbol{\gamma}_{j+1}, \phi_{j+1}), \quad \boldsymbol{\gamma}_{j+1} := \boldsymbol{\gamma}\big(x_{j+1}^+\big).$$

For the scheme defined by (3.18), Scheme 3, we cannot derive CFL conditions by enforcing a maximum principle like (3.13) or TVD property like (3.14). Nevertheless, we demonstrate in Section 4 that at least in one important case the scheme is stable and convergent if the following CFL conditions are satisfied:

$$\lambda \max_{j \in \mathbb{Z}_{\mathcal{J}}} v(\phi_j, \boldsymbol{\gamma}_j) \leq \alpha, \quad \lambda \max_{j \in \mathbb{Z}_{\mathcal{J}}} \phi_j \cdot \max_{j \in \mathbb{Z}_{\mathcal{J}}} \left| \partial_\phi v(\boldsymbol{\gamma}_j, \phi_j) \right| \leq \alpha, \quad \alpha = 1/2.$$

3.3. **Numerical flux for systems of conservation laws.** When generalizing the numerical flux to multi-species kinematic flows governed by (1.1) one should observe that only for the traffic and dispersion models, the velocities $v_i(\Phi)$ are always nonnegative; for the sedimentation model, the velocities $v_i(\Phi)$ are defined by (2.3) and may become negative due to buoyancy effects. This also occurs in the special case that all particles have the same density, and the velocities $v_i(\Phi)$ are defined by (2.9).

3.3.1. *Scheme 4 for systems ($N \geq 1$) with non-negative velocities.* In light of the above observation, for the multi-class traffic and the dispersion models a reasonable generalization of the scalar flux (3.8) is

$$(3.19) \qquad h_{i,j+1/2} = h_i(\Phi_{j+1}, \Phi_j) = \phi_{i,j} v_i(\Phi_{j+1}), \quad i = 1, \ldots, N.$$

We refer to the corresponding scheme as Scheme 4.

3.3.2. *Scheme 5 for systems ($N \geq 1$) with non-negative velocities and discontinuous flux.* As mentioned previously, for the multi-class traffic model, we are also interested in spatially varying velocities of the form (2.4). In that case we replace the numerical flux (3.19) by

$$(3.20) \qquad \begin{aligned} &h_{i,j+1/2} = h_i(k_{i,j+1}, \Phi_{j+1}, \Phi_j) = \phi_{i,j} v_{\max,j+1}^i V(\phi_{j+1}/\phi_{\max,j+1}), \\ &v_{\max,j+1}^i := v_{\max}^i\big(x_{j+1}^+\big), \quad \phi_{\max,j+1} := \phi_{\max}\big(x_{j+1}^+\big), \quad i = 1, \ldots, N \end{aligned}$$

(Scheme 5).

3.3.3. *Schemes 6, 7 and 8 for systems ($N \geq 1$) with velocities of variable sign.* For the sedimentation model, where the velocities may become negative, a potential generalization of the scalar numerical flux (3.9) is

$$(3.21) \qquad h_i(\Phi_{j+1}, \Phi_j) = \phi_{i,j} \max\{0, v_i(\Phi_{j+1})\} + \phi_{i,j+1} \min\{0, v_i(\Phi_{j+1})\}, \quad i = 1, \ldots, N$$

(Scheme 6), and for this flux, the numerical viscosity coefficients are given by

$$(3.22) \qquad Q_i(\Phi_{j+1}, \Phi_j) = \lambda |v_i(\Phi_{j+1})| + \lambda \phi_{i,j} \frac{v_i(\Phi_j) - v_i(\Phi_{j+1})}{\phi_{i,j+1} - \phi_{i,j}}.$$

Our numerical experiments with (3.19) give satisfactory results, and this is the first-order version of the flux that we use for systems where there are no negative velocities. When negative velocities are present, numerical experiments with (3.21) produce sharply resolved interfaces, but with overshoot in certain situations. To devise a numerical flux which overcomes this shortcoming, we return to the viscous formulation (3.10), (3.11) of the scalar numerical flux and observe that due to our assumption that $v(\cdot)$ is non-increasing, both terms on the right-hand side of (3.11) are nonnegative. In fact, we can rewrite (3.11) in the equivalent form

$$Q(\phi_{j+1}, \phi_j) = \lambda |v(\phi_{j+1})| + \lambda \phi_j \left| \frac{v(\phi_j) - v(\phi_{j+1})}{\phi_{j+1} - \phi_j} \right| = \lambda |v(\phi_{j+1})| + \lambda \phi_j \frac{|v(\phi_j) - v(\phi_{j+1})|}{\phi_{j+1} - \phi_j} \mathrm{sgn}(\phi_{j+1} - \phi_j).$$

Inserting this into (3.10) yields the following form of the scalar numerical flux (3.9):

$$(3.23) \quad h(\phi_{j+1}, \phi_j) = \frac{1}{2} \big(f(\phi_{j+1}) + f(\phi_j)\big) - \frac{1}{2} |v(\phi_{j+1})|(\phi_{j+1} - \phi_j) - \frac{\phi_j}{2} |v(\phi_j) - v(\phi_{j+1})| \mathrm{sgn}(\phi_{j+1} - \phi_j),$$

and this is the formulation that we generalize to systems when the velocities can become negative. In light of (3.23), a natural candidate for systems with velocities of both signs is

$$(3.24) \qquad \begin{aligned} h_i(\Phi_{j+1}, \Phi_j) &= \frac{1}{2} \big(\phi_{i,j+1} v_i(\Phi_{j+1}) + \phi_{i,j} v_i(\Phi_j)\big) - \frac{|v_i(\Phi_{j+1})|}{2}(\phi_{i,j+1} - \phi_{i,j}) \\ &\quad - \frac{\phi_{i,j}}{2} |v_i(\Phi_j) - v_i(\Phi_{j+1})| \mathrm{sgn}(\phi_{i,j+1} - \phi_{i,j}), \quad i = 1, \ldots, N, \end{aligned}$$

which defines Scheme 7. For this flux the numerical viscosity coefficient is

$$Q_i(\Phi_{j+1}, \Phi_j) = \lambda |v_i(\Phi_{j+1})| + \lambda \phi_{i,j} \left| \frac{v_i(\Phi_j) - v_i(\Phi_{j+1})}{\phi_{i,j+1} - \phi_{i,j}} \right|.$$

Our modification (3.24) to the numerical flux (3.19) consists of forcing the second term in the viscosity coefficient (3.22) to be positive. For scalar equations, this term is always positive, but this is not always true for systems. This modification is also potentially applicable to systems where all of the velocities are nonnegative, but we have found that the original flux (3.19) is satisfactory for such systems.

For polydisperse settling problems we find that (3.24) is an improvement over (3.21) but still sometimes gives non-physical overshoots at the interfaces between beds of sediment. For these problems we propose a slightly more viscous version of (3.24) that provides a good compromise between sharply resolved interfaces and suppression of overshoots:

$$\begin{aligned} h_i(\Phi_{j+1}, \Phi_j) &= \frac{1}{2} \big(\phi_{i,j+1} v_i(\Phi_{j+1}) + \phi_{i,j} v_i(\Phi_j)\big) - \frac{E_{j+1}}{2}(\phi_{i,j+1} - \phi_{i,j}) \\ &\quad - \frac{\phi_{i,j}}{2} |v_i(\Phi_j) - v_i(\Phi_{j+1})| \mathrm{sgn}(\phi_{i,j+1} - \phi_{i,j}), \quad i = 1, \ldots, N, \end{aligned}$$

which defines Scheme 8, and where $E_{j+1} := \max\{|v_1(\Phi_{j+1})|, \ldots, |v_N(\Phi_{j+1})|\}$.

3.4. **Invariant regions and CFL conditions for systems.** In Section 3.2 we derived CFL conditions by enforcing the TVD property and a very strong maximum principle. Both of these regularity properties are satisfied by the true solutions of the scalar conservation laws being approximated, but not generally for systems of conservation laws. In this section we derive CFL conditions for systems. We first derive the form of these CFL conditions by requiring that a certain invariant region be preserved. Once we have the form of the CFL conditions, we determine the constants on the right sides by referring to our scalar CFL conditions.

As discussed in Section 1.1, the problems of interest to us have a natural invariant region $\mathcal{D}_{\phi_{\max}}$ defined by (1.3). It is possible to show that our first-order scheme preserves this invariant region if we place some restrictions upon the velocity functions $v_i(\Phi)$. Since we also wish to allow for spatially varying coefficients, we generalize the definition (1.3), allowing it to vary spatially:

$$\mathcal{D}_{\phi_{\max,j}} := \left\{ \Phi = (\phi_1, \ldots, \phi_N)^{\mathrm{T}} \in \mathbb{R}^N : \ \phi_1 \geq 0, \ldots, \phi_N \geq 0, \ \phi := \phi_1 + \cdots + \phi_N \leq \phi_{\max,j} \right\}.$$

The following theorem applies to the multi-class traffic flow model discussed in Section 2.1.

Theorem 3.1. *Consider Scheme 5 defined by* (3.2) *with numerical flux* (3.20), *and either type of boundary conditions,* (3.4) *or* (3.5). *Assume that all velocity functions v_i are of the form* (2.4), *where $0 \leq v_{\max}^i(x) \leq \overline{v}_{\max}^i \leq \overline{v}_{\max}$ and $0 < \underline{\phi}_{\max} \leq \phi_{\max}(x) \leq \overline{\phi}_{\max}$, and that the hindrance factor $V(z)$ satisfies*

$$(3.25) \qquad 0 \leq V(z) \leq V_{\max}, \ V'(z) \leq 0, \ |V'(z)| \leq |V'|_{\max}, \ z \in [0,1]; \quad V(1) = 0.$$

Then if $\Phi_j^n \in \mathcal{D}_{\phi_{\max,j}}$ and the CFL conditions

$$(3.26) \qquad \lambda \overline{v}_{\max} V_{\max} \leq \alpha, \quad \lambda \left(\overline{\phi}_{\max} / \underline{\phi}_{\max} \right) \overline{v}_{\max} |V'|_{\max} \leq \alpha, \quad \alpha = 1$$

are satisfied at time level n, we will also have $\Phi_j^{n+1} \in \mathcal{D}_{\phi_{\max,j}}$.

Proof. Assume for now that the boundary conditions are periodic. The marching formula takes the form

$$(3.27) \qquad \phi_{i,j}^{n+1} = \phi_{i,j}^n - \lambda \phi_{i,j}^n v_{\max,j+1}^i V\left(\frac{\phi_{j+1}^n}{\phi_{\max,j+1}} \right) + \lambda \phi_{i,j-1}^n v_{\max,j}^i V\left(\frac{\phi_j^n}{\phi_{\max,j}} \right), \ i = 1, \ldots, N.$$

From this expression, it is clear that

$$\phi_{i,j}^{n+1} \geq \phi_{i,j}^n - \lambda \phi_{i,j}^n v_{\max,j+1}^i V\left(\frac{\phi_{j+1}^n}{\phi_{\max,j+1}} \right) = \left[1 - \lambda v_{\max,j+1}^i V\left(\frac{\phi_{j+1}^n}{\phi_{\max,j+1}} \right) \right] \phi_{i,j}^n$$

for $i = 1, \ldots, N$. This inequality implies that if $\Phi_j^n \in \mathcal{D}_{\phi_{\max,j}}$ for all $j \in \mathbb{Z}_{\mathcal{J}}$ we will have $\phi_{i,j}^{n+1} \geq 0$ if the first CFL condition appearing in (3.26) is satisfied.

Returning to the marching formula (3.27), we obtain that

$$\phi_{i,j}^{n+1} \leq \phi_{i,j}^n + \lambda \phi_{i,j-1}^n v_{\max,j}^i V\left(\frac{\phi_j^n}{\phi_{\max,j}} \right) \leq \phi_{i,j}^n + \lambda \phi_{i,j-1}^n \overline{v}_{\max} V\left(\frac{\phi_j^n}{\phi_{\max,j}} \right).$$

Summing over i gives

$$\phi_j^{n+1} \leq \phi_j^n + \lambda \sum_{i=1}^N \phi_{i,j-1}^n \overline{v}_{\max} V\left(\frac{\phi_j^n}{\phi_{\max,j}} \right) =: G(\phi_j^n).$$

Assumption (3.25) implies that $G(\phi_{\max,j}) = \phi_{\max,j}$. Moreover,

$$G'(\phi_j^n) = 1 + \lambda \sum_{i=1}^N \frac{\phi_{i,j-1}^n \overline{v}_{\max}}{\phi_{\max,j}} V'\left(\frac{\phi_j^n}{\phi_{\max,j}} \right).$$

From this expression we deduce that if the second of the CFL conditions appearing in (3.26) is satisfied, the function G will be a nondecreasing function of ϕ_j^n. Thus,

$$\max_{\phi_j^n \in [0, \phi_{\max,j}]} G(\phi_j^n) = G(\phi_{\max,j}) = \phi_{\max,j},$$

implying that $\phi_j^{n+1} \leq \phi_{\max,j}$. Finally, if the boundary conditions are of the zero-flux type, we only have to modify the proof at the two mesh points $j = 0$ and $j = \mathcal{J}$, where one of the flux contributions in (3.27) will be zero. Retracing the steps of the proof, we see that all inequalities remain valid. $\square$

It is common in traffic modeling to use a linear version of V, i.e., $V(z) = 1 - z$. In that case the CFL conditions (3.26) can be reduced to the single condition

$$(3.28) \qquad \lambda \left(\overline{\phi}_{\max} / \underline{\phi}_{\max} \right) \overline{v}_{\max} \leq \alpha, \quad \alpha = 1$$

and if $\phi_{\max}$ does not depend on x, i.e., $\phi_{\max}(x) \equiv \phi_{\max}$, this can be simplified even further to

$$(3.29) \qquad\qquad \lambda \overline{v}_{\max} \leq \alpha, \quad \alpha = 1.$$

The oil-in-water dispersion model of Section 2.3 does not quite fit the hypotheses of the previous theorem, but it is still possible to prove that the scheme preserves the invariant region $\mathcal{D}_{\phi_{\max}}$ if appropriate CFL conditions are enforced.

Theorem 3.2. *Consider Scheme 4 defined by* (3.2) *with numerical flux functions defined by* (3.19), *and zero-flux boundary conditions,* (3.5). *With the form of the velocities v_i for the oil-in-water dispersion model specified in Section 2.3, if $\Phi_j^n \in \mathcal{D}_{\phi_{\max}}$ (here $\phi_{\max} = 1$) and the CFL conditions*

$$(3.30) \qquad \lambda v_i(\Phi_j^n) \leq \alpha, \quad i = 1, \dots, N, \quad j \in \mathbb{Z}_{\mathcal{J}}, \quad \lambda \frac{c}{\mu_{\mathrm{d}}(\Phi_j^n)} \sum_{i=1}^{N} \phi_{i,j-1}^n \mathcal{V}_i^{2/3} \leq \alpha, \quad \alpha = 1, \quad j \in \mathbb{Z}_{\mathcal{J}}$$

are satisfied, then $\Phi_j^{n+1} \in \mathcal{D}_{\phi_{\max}}$.

Proof. First take the case where the boundary condition is not involved, $0 < j < \mathcal{J}$ (an interior point). The marching formula then takes the form

$$(3.31) \qquad\qquad \phi_{i,j}^{n+1} = \phi_{i,j}^n - \lambda \phi_{i,j}^n v_i(\Phi_{j+1}^n) + \lambda \phi_{i,j-1}^n v_i(\Phi_j^n), \quad i = 1, \dots, N.$$

This expression implies that

$$\phi_{i,j}^{n+1} \geq \phi_{i,j}^n - \lambda \phi_{i,j}^n v_i(\Phi_{j+1}^n) = \left(1 - \lambda v_i(\Phi_{j+1}^n)\right) \phi_{i,j}^n, \quad i = 1, \dots, N.$$

Using this inequality, along with the first CFL condition in (3.30), we conclude that if $\phi_{i,j}^{n+1} \geq 0$. The marching formula (3.31) also implies that $\phi_{i,j}^{n+1} \leq \phi_{i,j}^n + \lambda \phi_{i,j-1}^n v_i(\Phi_j^n)$. Summing over i gives

$$\phi_j^{n+1} \leq \phi_j^n + \lambda \sum_{i=1}^{N} \phi_{i,j-1}^n v_i(\Phi_j^n) =: G(\Phi_j^n).$$

To simplify notation, we write G as

$$G(\Phi) = \phi + \lambda \sum_{i=1}^{N} \psi_i \, v_i(\Phi), \quad \Phi = \Phi_j^n, \quad \phi = \phi_j^n, \quad \psi_i = \phi_{i,j-1}^n.$$

Recalling that for this model $\phi_{\max} = 1$, we complete the proof by showing that

$$(3.32) \qquad\qquad \max_{\Phi \in \mathcal{D}_{\phi_{\max}}} G(\Phi) \leq 1.$$

From (2.10), we obtain that

$$(3.33) \qquad\qquad G(\Phi) = \phi + \lambda B \cdot \frac{1 - \phi}{\mu_{\mathrm{d}}(\Phi)}, \quad B := c \sum_{i=1}^{N} \psi_i \, \mathcal{V}_i^{2/3}.$$

Rearranging (3.33) and using $\phi \leq \phi_{\max} = 1$ yields

$$G(\Phi) = \left(1 - \lambda \frac{B}{\mu_{\mathrm{d}}(\Phi)}\right) \phi + \lambda \frac{B}{\mu_{\mathrm{d}}(\Phi)} \leq 1.$$

To obtain the last inequality, we have used the second CFL condition appearing in (3.30). Thus, (3.32) is valid, and the proof is complete for each interior point. To complete the proof, we must deal with the remaining mesh points x_0 and $x_{\mathcal{J}}$. At x_0, the marching formula (3.31) simplifies to

$$(3.34) \qquad\qquad \phi_{i,0}^{n+1} = \phi_{i,0}^n - \lambda \phi_{i,0}^n v_i(\Phi_1^n), \quad i = 1, \dots, N.$$

That $\phi_{i,0}^{n+1} \geq 0$ now follows from the CFL condition exactly as in the case of an interior point. For the upper bound, it is immediate by summing over i in (3.34) that $\phi_0^{n+1} \leq \phi_0^n$, and thus $\Phi_0^{n+1} \in \mathcal{D}_{\phi_{\max}}$. At $x_{\mathcal{J}}$, the marching formula (3.31) becomes

$$(3.35) \qquad\qquad \phi_{i,\mathcal{J}}^{n+1} = \phi_{i,\mathcal{J}}^n + \lambda \phi_{i,\mathcal{J}-1}^n v_i(\Phi_{\mathcal{J}}^n), \quad i = 1, \dots, N.$$

Now the proof that $\phi_{i,\mathcal{J}} \geq 0$ is clear from (3.35), and the upper bound $\phi_{\mathcal{J}}^{n+1} \in \mathcal{D}_{\phi_{\max}}$ follows exactly as in the proof above for an interior point. $\qquad\square$

In light of (2.10), the maximum velocities are given by $v_{\max}^i = c\mathcal{V}_i^{2/3}/\mu_{\mathrm{f}}$. Using these maximum velocities, it is possible to combine the CFL conditions (3.30) for the oil-in-water dispersion model into the single and simplified, but possibly more restrictive, condition

$$(3.36) \qquad \lambda \max_{i=1,\ldots,N} v_{\max}^i \leq \alpha, \quad \alpha = 1.$$

In the scalar case ($N = 1$), the CFL conditions (3.26) and (3.30) are essentially the CFL conditions (3.16), except with Courant number $\alpha = 1$ instead of $1/2$. The smaller $\alpha = 1/2$ on the right side of (3.16) can be explained by the fact that those conditions were derived in order to enforce both a TVD property and a more restrictive local maximum principle. The non-oscillatory property of our scalar scheme is due to the TVD property. Since we wish to extend this property to the systems version of our scheme, in practice we use the more restrictive Courant number $\alpha = 1/2$ in (3.26) for the multi-class traffic model. Similarly, we use $\alpha = 1/2$ in the CFL condition (3.30) for the scheme as it applies to the oil-in-water dispersion model. Finally, we replace Courant number $\alpha = 1$ by $\alpha = 1/2$ in the simplified single CFL conditions (3.28) and (3.29) and the simplified single CFL condition (3.36) for the oil-in-water model.

For the multi-class traffic model and the oil-in-water dispersion model, we have found the form that CFL conditions should take by enforcing certain invariant regions, and then modifying the parameter on the right side of the CFL inequalities by referring back to simpler scalar conservation laws. For the polydisperse sedimentation model, we do not currently have a proof that our scheme preserves the invariant region $\mathcal{D}_{\phi_{\max}}$, so we can not directly carry out such a program. However, based on our analysis of the simpler multi-class traffic and oil-in-water dispersion models, the CFL condition of the following type seems reasonable for the polydisperse sedimentation model:

$$(3.37) \qquad \lambda \max_{i=1,\ldots,N} |v^i|_{\max} \leq \alpha, \quad \alpha = 1/2, \quad |v^i|_{\max} := \max_{\Phi \in \mathcal{D}_{\phi_{\max}}} |v_i(\Phi)|.$$

Due to the complicated form of the velocities v_i for the polydisperse sedimentation model, these maximum velocities may be difficult to calculate. As an alternative, we can replace the CFL condition (3.37) by

$$\lambda_n \max_{j \in \mathbb{Z}_\mathcal{J}} \max_{i=1,\ldots,N} |v_i(\Phi_j^n)| \leq \alpha, \quad \alpha = 1/2.$$

We enforce this CFL condition by computing at each time level

$$\lambda_n = \frac{1}{2\max_{j \in \mathbb{Z}_\mathcal{J}} \max_{i=1,\ldots,N} |v_i(\Phi_j^n)|},$$

and then computing the time step via $\Delta t_n = \lambda_n \Delta x$. Our numerical experiments indicate that this approach works well.

3.5. **Higher-order versions (Schemes 9 and 10).** Schemes 1 to 8 are only first-order accurate, meaning that a very fine mesh is required in order to accurately resolve some features of the solution. To improve on this situation, we propose a formally second-order scheme, constructed by using MUSCL [67] spatial differencing, and Runge-Kutta temporal differencing. The MUSCL version of the ith flux component reads

$$(3.38) \qquad h_i^{\mathrm{m}}(\gamma_{i,j+1}, \Phi_{j+2}, \Phi_{j+1}, \Phi_j, \Phi_{j-1}) = h_i\left(\gamma_{i,j+1}, \Phi_{j+1} - \frac{1}{2}\sigma_{j+1}, \Phi_j + \frac{1}{2}\sigma_j\right),$$

$$(3.39) \qquad \gamma_{i,j+1} := \gamma_i(x_{j+1}^+), \quad i = 1,\ldots,N,$$

where h_i is the first-order version of the flux, and we define the slope vector $\sigma_j := (\sigma_{1,j},\ldots,\sigma_{N,j})^{\mathrm{T}}$ with

$$(3.40) \qquad \sigma_{i,j} = \begin{cases} \mathrm{minmod}\{\phi_{i,j+1} - \phi_{i,j}, \phi_{i,j} - \phi_{i,j-1}\} & \text{if } j = 1,\ldots,J-1, \\ 0 & \text{if } j = 0 \text{ or } j = J, \end{cases} \quad i = 1,\ldots,N,$$

where, as usual, $\mathrm{minmod}\{a, b\} := (\mathrm{sgn}(a) + \mathrm{sgn}(b))\min\{|a|, |b|\}/2$, or the less dissipative Van Leer limiter

$$(3.41) \qquad \sigma_{i,j} = \begin{cases} \Theta_{i,j} & \text{if } j = 1, \ldots, J-1, \\ 0 & \text{if } j = 0 \text{ or } j = J, \end{cases} \quad i = 1, \ldots, N,$$

$$\Theta_{i,j} := \frac{|\phi_{i,j} - \phi_{i,j-1}|(\phi_{i,j+1} - \phi_{i,j}) + |\phi_{i,j+1} - \phi_{i,j}|(\phi_{i,j} - \phi_{i,j-1})}{|\phi_{i,j} - \phi_{i,j-1}| + |\phi_{i,j+1} - \phi_{i,j}|}.$$

When the boundary conditions are of the zero-flux type, we simply set $\boldsymbol{\sigma}_j = 0$ when $j = 0, \mathcal{J}$. In the scalar case, this avoids non-physical overshoot that can occur otherwise.

In all examples in this paper, the parameter $\boldsymbol{\gamma}$ is piecewise constant. If $\boldsymbol{\gamma}$ is piecewise smooth, it is necessary to use $\boldsymbol{\gamma}_{i,j+1/2} := \boldsymbol{\gamma}_i(x^+_{j+1/2})$ in (3.38) instead of $\boldsymbol{\gamma}_{i,j+1}$ in order to achieve second-order accuracy. Some care is required here in order to avoid non-physical overshoots at jumps in $\boldsymbol{\gamma}$. A simple way to avoid such overshoots is to use $\boldsymbol{\gamma}_{j+1}$ instead of $\boldsymbol{\gamma}_{j+1/2}$ when there is a jump in $\boldsymbol{\gamma}$ between x_j and x_{j+1}. Note that in any case we are not attempting to achieve higher than first-order accuracy at the location of jumps in $\boldsymbol{\gamma}$.

Consequently, away from the boundaries, the MUSCL scheme is formally second-order accurate in space, but not in time. To achieve formal second-order accuracy in time also, we use second-order Runge-Kutta (RK) time stepping. More specifically, if we write our scheme with first-order Euler time differencing and second-order spatial differencing abstractly as

$$(3.42) \qquad \Phi^{n+1}_j = \Phi^n_j - \Gamma_j\big(\Phi^n_{j+2}, \Phi^n_{j+1}, \Phi^n_j, \Phi^n_{j-1}, \Phi^n_{j-2}\big),$$

then the RK version takes the following two-step form

$$(3.43) \qquad \begin{aligned} \tilde{\Phi}^{n+1}_j &= \Phi^n_j - \Gamma_j\left(\Phi^n_{j+2}, \Phi^n_{j+1}, \Phi^n_j, \Phi^n_{j-1}, \Phi^n_{j-2}\right), \\ \Phi^{n+1}_j &= \frac{1}{2}\Phi^n_j + \frac{1}{2}\tilde{\Phi}^{n+1}_j - \frac{1}{2}\Gamma_j\big(\tilde{\Phi}^{n+1}_{j+2}, \tilde{\Phi}^{n+1}_{j+1}, \tilde{\Phi}^{n+1}_j, \tilde{\Phi}^{n+1}_{j-1}, \tilde{\Phi}^{n+1}_{j-2}\big). \end{aligned}$$

This type of time discretization is formally second-order accurate in time, Strong Stability Preserving (SSP), see [68], and does not require any additional reduction of the allowable time step. We refer to the scheme based on the first-order flux (3.8) and extended to second-order in space and time accuracy by (3.38), (3.40) and (3.42), (3.43), respectively, as Scheme 9, while the variant that uses the Van Leer limiter (3.41) (instead of (3.40)) as Scheme 10.

Theorem 3.3. *Consider the scalar initial value problem with flux* (3.6) *and periodic boundary conditions. Assume that* $v'(\phi) \leq 0$, $v(\phi) \geq 0$, $v(\phi_{\max}) = 0$, $v(0) = v_{\max}$. *Assume that the initial data satisfies* $\phi_0(x) \in [0, \phi_{\max}]$, $TV(\phi_0) < \infty$. *Then Schemes 9 and 10 produce approximations that satisfy the maximum principle* (3.13) *and TVD property* (3.14) *if the CFL condition* (3.16) *is satisfied and the slopes* σ_j *satisfy*

$$(3.44) \qquad 0 \leq \frac{\sigma_j}{2\Delta_+\phi_j} \leq 1, \quad 0 \leq \frac{\sigma_j}{2\Delta_-\phi_j} \leq 1.$$

Remark 3.1. The main point of the preceding theorem is that we do not have to reduce the allowable time step when using the second-order scheme. Also, note that both the minmod limiter and the Van Leer limiter enforce the inequalities (3.44).

Proof. Since the RK processing does not affect the stability properties, we carry out the proof for the scheme where only the MUSCL processing is included. Following [69], we write the scheme in incremental form

$$\phi^{n+1}_j = \phi^n_j + C^n_{j+1/2}\Delta_+\phi^n_j - D^n_{j-1/2}\Delta_-\phi^n_j,$$

where

$$C^n_{j+1/2} = \frac{-\lambda}{\Delta_+\phi^n_j}\left[\left(\phi^n_j + \frac{\sigma^n_j}{2}\right)v\left(\phi^n_{j+1} - \frac{\sigma^n_{j+1}}{2}\right) - \left(\phi^n_j + \frac{\sigma^n_j}{2}\right)v\left(\phi^n_j - \frac{\sigma^n_j}{2}\right)\right],$$

$$D^n_{j-1/2} = \frac{\lambda}{\Delta_-\phi^n_j}\left[\left(\phi^n_j + \frac{\sigma^n_j}{2}\right)v\left(\phi^n_j - \frac{\sigma^n_j}{2}\right) - \left(\phi^n_{j-1} + \frac{\sigma^n_{j-1}}{2}\right)v\left(\phi^n_j - \frac{\sigma^n_j}{2}\right)\right].$$

A straightforward calculation gives

$$(3.45) \qquad C_{j+1/2}^n = -\lambda \left(\phi_j^n + \frac{\sigma_j^n}{2} \right) v'\left(\xi_{j+1/2}^n\right) \left[1 - \frac{\sigma_{j+1}^n}{2\Delta_+ \phi_j^n} + \frac{\sigma_j^n}{2\Delta_+ \phi_j^n} \right],$$

$$(3.46) \qquad D_{j-1/2}^n = \lambda v \left(\phi_j^n - \frac{\sigma_j^n}{2} \right) \left[1 + \frac{\sigma_j^n}{2\Delta_- \phi_j^n} - \frac{\sigma_{j-1}^n}{2\Delta_- \phi_j^n} \right].$$

The assumptions on ϕ_0 imply $\phi_j^0 \in [0, \phi_{\max}]$ and $TV(\phi^0) < \infty$. Assume that $\phi_j^n \in [0, \phi_{\max}]$ and $TV(\phi^n) < \infty$ also hold. Thanks to (3.44), the bracketed terms in (3.45) and (3.46) are nonnegative. The requirement (3.44) also implies that the quantities $\phi_j^n \pm \sigma_j^n/2$ are contained in the interval $[0, \phi_{\max}]$. With these observations, it is clear that $C_{j+1/2}^n \geq 0$ and $D_{j-1/2}^n \geq 0$.

Finally, (3.44) implies that the bracketed terms in (3.45) and (3.46) do not exceed 2. Combining this fact with the CFL condition (3.16), it is clear that $C_{j+1/2}^n \leq 1/2$ and $D_{j-1/2}^n \leq 1/2$. Thus $C_{j+1/2}^n + D_{j+1/2}^n \leq 1$ and $C_{j+1/2}^n + D_{j-1/2}^n \leq 1$. Combining these inequalities with the non-negativity of $C_{j+1/2}^n$ and $D_{j+1/2}^n$ proves that $\phi_j^{n+1} \in [0, \phi_{\max}]$, and $TV(\phi^{n+1}) < \infty$, and thus the proof is complete by induction on n. $\qquad\square$

4. Convergence analysis

In this section we focus on the scalar initial value problem with periodic boundary conditions:

$$(4.1) \qquad \begin{aligned} &\phi_t + \big(k(x)\phi V(\phi/\phi_{\max})\big)_x = 0, \quad (x,t) \in [0, L] \times (0, T) =: \Pi_T \\ &\phi(x, 0) = \phi_0(x), \\ &\phi(0, t) = \phi(L, t), \end{aligned}$$

with the initial datum ϕ_0 satisfying

$$(4.2) \qquad \phi_0 \in BV([0, L]) \cap L^1([0, L]) \cap L^\infty([0, L]), \quad \phi_0(x) \in [0, \phi_{\max}] \text{ for all } x \in [0, L].$$

We assume that the coefficient k is positive, bounded, and piecewise constant:

$$(4.3) \qquad 0 < k_{\min} \leq k(x) \leq k_{\max}, \quad \exists \xi_1, \ldots, \xi_M \in (0, L) : k|_{(\xi_m, \xi_{m+1})} \equiv k_m.$$

Note that the coefficient k has jumps at the points ξ_m.

Let $f(\phi) := \phi V(\phi/\phi_{\max})$. We assume that $V : [0, 1] \mapsto [0, V_{\max}]$ is C^1, satisfies (3.25), and that

$$(4.4) \qquad \exists \phi^* \in (0, \phi_{\max}) : f'(\phi) > 0 \text{ for } \phi \in (0, \phi^*) \text{ and } f'(\phi) < 0 \text{ for } \phi \in (\phi^*, \phi_{\max}).$$

This last condition is satisfied if for example, $V(z) = (1 - z)^n$, where $n \geq 1$.

This is a simple scalar model of traffic flow discussed in Section 2.1. Relating this to (2.2)–(2.4), we obtain the scalar velocity $v(x, \phi) = k(x)V(\phi/\phi_{\max})$. The parameter $k(x)$ is playing the role of $v_{\max}^1(x)$; we make this change to simplify the notation in this section. Also, we take $\phi_{\max}$ to be constant in this section. With this simplification, along with the other assumptions stated above, the problem is a well-studied one.

Definition 4.1 (BV_t entropy solution). *A measurable function $\phi : \Pi_T \to \mathbb{R}$ is a BV_t entropy solution of the initial value problem (4.1) if*

$$(4.5) \qquad \phi \in L^1(\Pi_T) \cap BV_t(\Pi_T) \cap L^\infty(\Pi_T), \qquad \phi(x, t) \in [0, \phi_{\max}] \quad \text{for a.e. } (x, t) \in \Pi_T;$$

the following Kružkov-type entropy inequality holds for any $\psi \in \mathcal{D}(\Pi_T)$, $\psi \geq 0$, $\psi(0, t) = \psi(L, t)$:

$$\iint_{\Pi_T} \left(|\phi - c| \, \partial_t \psi + \mathrm{sgn}(\phi - c)\big(k(x)f(\phi) - k(x)f(c)\big)\partial_x \psi \right) dt \, dx$$

$$+ \int_0^T \sum_{m=0}^M \left| k\big(\xi_m^+\big) - k\big(\xi_m^-\big) \right| f(c)\psi(\xi_m, t) \, dt \geq 0 \qquad \forall c \in \mathbb{R};$$

and the initial condition is satisfied in the following strong L^1 sense:

$$(4.6) \qquad \operatorname*{ess\,lim}_{t \downarrow 0} \int_{\mathbb{R}} \left| \phi(x, t) - \phi_0(x) \right| dx = 0.$$

Due to our assumptions on the flux f and the coefficient k, there is a well-developed uniqueness and existence theory for the problem (4.1). In particular, by combining the results of [37] and [38], we have

Theorem 4.1. *Problem* (4.1) *with assumptions* (4.2)–(4.4) *has a unique* BV_t *entropy solution in the sense of Definition* 4.1.

To construct approximate solutions to the initial value problem (4.1) we discretize Π_T as in Section 3.1, and use the marching formula

$$(4.7) \qquad \phi_j^{n+1} = \phi_j^n - \lambda\big(h_{j+1/2}^n - h_{j-1/2}^n\big), \quad h_{j+1/2}^n := k_{j+1}\phi_j^n V(\phi_{j+1}^n/\phi_{\max}).$$

Here the flux $h_{j+1/2}^n$ is defined by (3.18) (Scheme 3), as applied to the assumptions of this section.

To simplify the analysis, we choose a uniform time step $\Delta t_n = \Delta t$ such that the CFL condition

$$(4.8) \qquad \lambda k_{\max} V_{\max} \le \alpha, \quad \lambda k_{\max} |V'|_{\max} \le \alpha, \quad \alpha = 1/2$$

is satisfied. This is the version of (3.26) that applies to the present situation. We extend the grid function ϕ_j^n so that it is defined on all of Π_T via

$$\phi^\Delta(x,t) = \sum_{n=0}^{\mathcal{N}} \sum_{j=0}^{\mathcal{J}} \phi_j^n \chi_j(x)\chi_n(t),$$

where $\chi_j(x)$ is the characteristic function for the spatial interval $[x_j - \Delta x/2, x_j + \Delta x/2)$ and $\chi_n(t)$ is the characteristic function for the temporal interval $[t_n, t_n + \Delta t)$.

Lemma 4.1. *Scheme 3 is monotone in the sense that if* $\{\phi_j^n\}$ *and* $\{\sigma_j^n\}$ *are two approximate solutions lying in the interval* $[0, \phi_{\max}]$ *such that* $\phi_j^n \le \sigma_j^n$ *for all* $j \in \mathcal{J}$, *then* $\phi_j^{n+1} \le \sigma_j^{n+1}$ *for all* $j \in \mathcal{J}$. *Furthermore, if the initial data* $\phi_0(x)$ *lies in the interval* $[0, \phi_{\max}]$ *for all* $x \in [0, L]$, *then the computed approximation also satisfies* $\phi_j^n \in [0, \phi_{\max}]$ *for all* $n \ge 0$ *and all* $j \in \mathcal{J}$. *In addition, we have the discrete time continuity estimate*

$$(4.9) \qquad \sum_{j=0}^{\mathcal{J}} \big|\phi_j^{n+1} - \phi_j^n\big| \le C, \quad n = 0, 1, \ldots, \mathcal{N},$$

where the constant C *is independent of the mesh size* Δ *and the time level* n.

Proof. Substituting the formula for the numerical flux into the marching formula (4.7) and then taking partial derivatives yields

$$\frac{\partial \phi_j^{n+1}}{\partial \phi_{j+1}^n} = -\frac{\lambda k_{j+1}\phi_j^n}{\phi_{\max}} V'\left(\frac{\phi_{j+1}^n}{\phi_{\max}}\right), \quad \frac{\partial \phi_j^{n+1}}{\partial \phi_{j-1}^n} = \lambda k_j V(\phi_j^n/\phi_{\max}),$$

$$\frac{\partial \phi_j^{n+1}}{\partial \phi_j^n} = 1 - \lambda k_{j+1} V\left(\frac{\phi_{j+1}^n}{\phi_{\max}}\right) + \frac{\lambda k_j \phi_{j-1}^n}{\phi_{\max}} V'\left(\frac{\phi_j^n}{\phi_{\max}}\right).$$

That the first two partial derivatives are nonnegative is obvious. The third one is nonnegative thanks to the CFL condition. The first assertion is now an immediate consequence of the non-negativity of these partial derivatives. For the second assertion, note that if we apply the scheme to the constant data $p_j^0 \equiv 0$ and $q_j^0 \equiv \phi_{\max}$, the result is $p_j^1 \equiv 0$ and $q_j^1 \equiv \phi_{\max}$. Since $0 = p_j^0 \le \phi_j^0 \le q_j^0 \le \phi_{\max}$, we will have $0 = p_j^1 \le \phi_j^1 \le q_j^1 \le \phi_{\max}$; this follows from the monotonicity. Continuing this way by induction completes the proof of the second assertion. The third assertion (4.9) is basically a consequence of the Crandall-Tartar lemma [64], along with the boundedness of the variation of the initial data. The proof is very similar to that of [37, Lemma 3.3], so we omit the details. $\qquad \square$

In order to establish compactness, we a need a spatial variation bound, which is provided by the following lemma. Let $V_a^b(z)$ denote the total variation of the function $x \mapsto z(x)$ over the interval $[a, b]$.

Lemma 4.2. *For any interval* $[a, b]$ *such that* $\{\xi_1, \ldots, \xi_M\} \cap [a, b] = \emptyset$, *and any* $t \in [0, T]$ *we have a spatial variation bound of the form* $V_a^b(\phi^\Delta(\cdot, t)) \le C(a, b)$, *where* $C(a, b)$ *is independent of* Δ *and* t *for* $t \in [0, T]$.

Proof. Due to our time continuity estimate (4.9), there is a constant K such that

$$(4.10) \qquad \Delta x \sum_{j=0}^{\mathcal{J}} \sum_{n=0}^{\mathcal{N}} \left| \phi_j^{n+1} - \phi_j^n \right| \leq K.$$

Since $\{\xi_1, \dots, \xi_M\} \cap [a, b] = \emptyset$, we can assume that there is an index m such that $\xi_m < a < b < \xi_{m+1}$. Fix $r > 0$, and without loss of generality, assume that $r > \Delta x$ for all mesh sizes Δx of interest. Let

$$\mathcal{A} := \mathcal{A}(\Delta) := \{ j \,|\, x_j \in [a - r - \Delta x, a] \}, \quad \mathcal{B} := \mathcal{B}(\Delta) := \{ j \,|\, x_j \in [b, b + r + \Delta x] \},$$

and observe that $|\mathcal{A}| \Delta x \geq r$, $|\mathcal{B}| \Delta x \geq r$. It is then clear from (4.10) that

$$(4.11) \qquad \Delta x \sum_{j \in \mathcal{A}} \sum_{n=0}^{\mathcal{N}} \left| \phi_j^{n+1} - \phi_j^n \right| \leq K, \quad \Delta x \sum_{j \in \mathcal{B}} \sum_{n=0}^{\mathcal{N}} \left| \phi_j^{n+1} - \phi_j^n \right| \leq K.$$

We can choose $j_a = j_a(\Delta)$, $j_b = j_b(\Delta)$ with $j_a \in \mathcal{A}$, $j_b + 1 \in \mathcal{B}$ such that

$$\sum_{n=0}^{\mathcal{N}} \left| \phi_{j_a}^{n+1} - \phi_{j_a}^n \right| = \min_{j \in \mathcal{A}} \sum_{n=0}^{\mathcal{N}} \left| \phi_j^{n+1} - \phi_j^n \right|, \quad \sum_{n=0}^{\mathcal{N}} \left| \phi_{j_b+1}^{n+1} - \phi_{j_b+1}^n \right| = \min_{j \in \mathcal{B}} \sum_{n=0}^{\mathcal{N}} \left| \phi_j^{n+1} - \phi_j^n \right|.$$

It follows from (4.11) that

$$(4.12) \qquad \sum_{n=0}^{\mathcal{N}} \left| \phi_{j_a}^{n+1} - \phi_{j_a}^n \right| \leq \frac{K}{|\mathcal{A}| \Delta x} \leq \frac{K}{r}, \quad \sum_{n=0}^{\mathcal{N}} \left| \phi_{j_b+1}^{n+1} - \phi_{j_b+1}^n \right| \leq \frac{K}{|\mathcal{B}| \Delta x} \leq \frac{K}{r}.$$

Due to the way that we selected j_a and j_b, for $j_a \leq j \leq j_b$ we can write the scheme as

$$(4.13) \qquad \phi_j^{n+1} = \phi_j^n - k_m \lambda \Delta_- \bar{f}(\phi_{j+1}^n, \phi_j^n), \quad \bar{f}(\phi_{j+1}^n, \phi_j^n) := \phi_j^n V(\phi_{j+1}^n / \phi_{\max}).$$

The formula (4.13) can also be written in incremental form

$$(4.14) \qquad \phi_j^{n+1} = \phi_j^n + C_{j+1/2}^n \Delta_+ \phi_j^n - D_{j-1/2}^n \Delta_- \phi_j^n,$$

where

$$C_{j+1/2}^n = \lambda k_m \frac{f(\phi_j^n) - \bar{f}(\phi_{j+1}^n, \phi_j^n)}{\Delta_+ \phi_j^n}, \quad D_{j-1/2}^n = \lambda k_m \frac{f(\phi_j^n) - \bar{f}(\phi_j^n, \phi_{j-1}^n)}{\Delta_- \phi_j^n}.$$

Using the definitions of f and $\bar{f}$, and invoking the CFL condition (4.8), it is easy to check that

$$(4.15) \qquad C_{j+1/2}^n \geq 0, \quad D_{j+1/2}^n \geq 0, \quad C_{j+1/2}^n + D_{j+1/2}^n \leq 1.$$

The incremental form (4.14) implies that the differences evolve according to

$$(4.16) \qquad \Delta_+ \phi_j^{n+1} = \Delta_+ \phi_j^n + C_{j+3/2}^n \Delta_+ \phi_{j+1}^n - C_{j+1/2}^n \Delta_+ \phi_j^n - D_{j+1/2}^n \Delta_+ \phi_j^n + D_{j-1/2}^n \Delta_- \phi_j^n.$$

Note that when $j = j_a$, we can write (4.16) as

$$(4.17) \qquad \Delta_+ \phi_{j_a}^{n+1} = \Delta_+ \phi_{j_a}^n + C_{j_a+3/2}^n \Delta_+ \phi_{j_a+1}^n - D_{j_a+1/2}^n \Delta_+ \phi_{j_a}^n - \left(\phi_{j_a}^{n+1} - \phi_{j_a}^n \right).$$

Similarly, when $j = j_b$, (4.16) takes the form

$$(4.18) \qquad \Delta_+ \phi_{j_b}^{n+1} = \Delta_+ \phi_{j_b}^n - C_{j_b+1/2}^n \Delta_+ \phi_{j_b}^n + D_{j_b-1/2}^n \Delta_- \phi_{j_b}^n + \left(\phi_{j_b+1}^{n+1} - \phi_{j_b+1}^n \right).$$

Taking absolute values and summing over j in (4.16), we use the properties (4.15) to proceed as in the proof of Harten's lemma (Lemma 2.2 of [65]). To deal with the boundary contributions, we use (4.17) and

(4.18). This calculation yields

$$\sum_{j=j_a}^{j_b} \left|\Delta_+\phi_j^{n+1}\right| \le \left(1 - D_{j_a+1/2}^n\right)\left|\Delta_+\phi_{j_a}^n\right| + C_{j_a+3/2}^n\left|\Delta_+\phi_{j_a+1}^n\right| + \left|\phi_{j_a}^{n+1} - \phi_{j_a}^n\right|$$

$$+ \sum_{j=j_a+1}^{j_b-1}\left(1 - C_{j+1/2}^n - D_{j+1/2}^n\right)\left|\Delta_+\phi_j^n\right| + \sum_{j=j_a+1}^{j_b-1} C_{j+3/2}^n\left|\Delta_+\phi_{j+1}^n\right|$$

$$+ \sum_{j=j_a+1}^{j_b-1} D_{j-1/2}^n\left|\Delta_-\phi_j^n\right| + \left(1 - C_{j_b+1/2}\right)\left|\Delta_+\phi_{j_b}^n\right| + D_{j_b-1/2}^n\left|\Delta_-\phi_{j_b}^n\right| + \left|\phi_{j_a}^{n+1} - \phi_{j_a}^n\right|$$

$$\le \sum_{j=j_a}^{j_b}\left|\Delta_+\phi_j^n\right| + \left|\phi_{j_a}^{n+1} - \phi_{j_a}^n\right| + \left|\phi_{j_b+1}^{n+1} - \phi_{j_b+1}^n\right|.$$

Proceeding by induction, and then using (4.12), we find that for $1 \le n \le \mathcal{N}$

$$(4.19) \qquad \sum_{j=j_a}^{j_b}\left|\Delta_+\phi_j^n\right| \le \sum_{j=j_a}^{j_b}\left|\Delta_+\phi_j^0\right| + \sum_{\nu=1}^n\left(\left|\phi_{j_a}^\nu - \phi_{j_a}^{\nu-1}\right| + \left|\phi_{j_b+1}^\nu - \phi_{j_b+1}^{\nu-1}\right|\right) \le \sum_{j=j_a}^{j_b}\left|\Delta_+\phi_j^0\right| + \frac{2K}{r}.$$

The proof is completed with the observation that $[a, b] \subseteq [x_{j_a}, x_{j_b+1}]$, along with the assumption that u_0 has bounded variation. $\qquad\square$

Remark 4.1. Note that the spatial variation bound provided by Lemma 4.2 is only local, and due to the term $2K/r$ appearing in (4.19), it blows up if the distance from one of the endpoints of the interval $[a, b]$ to one of the jump points ξ_m or ξ_{m+1} approaches zero. This is consistent with the fact that there is currently no known global spatial variation bound for conservation laws of this type (i.e., with a discontinuous coefficient). This has made it necessary to use alternative approaches to prove compactness, including the singular mapping approach, and the compensated compactness approach. The local variation bound established above provides one more analytical tool for such problems.

We state the following lemma without proof; it follows from the monotonicity property (Lemma 4.1), and is based on a discrete entropy inequality due to Crandall and Majda [64] which was later adapted to the situation where there are discontinuous coefficients, see [37] or [38].

Lemma 4.3. *For any $c \in \mathbb{R}$, the following cell entropy inequality is satisfied by approximate solutions ϕ_j^n generated by the scheme (4.7) (Scheme 3):*

$$\left|\phi_j^{n+1} - c\right| \le \left|\phi_j^n - c\right| - \lambda\,\Delta_- H_{j+1/2}^n + \lambda\left|k_{j+1} - k_j\right| f(c),$$

where the numerical entropy flux $H_{j+1/2}^n$ is defined by

$$H_{j+1/2}^n = k_{j+1}\bar{f}\left(\phi_{j+1}^n \vee c, \phi_j^n \vee c\right) - k_{j+1}\bar{f}\left(\phi_{j+1}^n \wedge c, \phi_j^n \wedge c\right),$$

and $\bar{f}$ is defined in (4.13).

Theorem 4.2. *Let the function ϕ^Δ be defined by (4.7) (Scheme 3). Assume that $\Delta := (\Delta x, \Delta t) \to 0$ with the ratio λ fixed and satisfying the CFL condition (4.8). Then $\phi^\Delta \to \phi$ boundedly a.e. and in $L^1(\Pi_T)$, where ϕ is the unique BV_t entropy solution to the initial value problem (4.1) in the sense of Definition 4.1.*

Proof. For our approximate solutions ϕ^Δ, Lemma 4.1 gives us an L^∞ bound and a time continuity bound. Since our spatial domain $[0, L]$ is compact, a uniform L^1 bound follows immediately from our L^∞ bound. We also have a bound on the spatial variation in any interval $[a, b]$ not containing any of the points $\xi_1, \dots, \xi_M$.

By standard compactness results, for any set $\mathcal{S}$ of the form

$$(4.20) \qquad \mathcal{S} = \bigcup_{p=1}^P [a_p, b_p], \quad \mathcal{S} \cap \{\xi_1, \dots, \xi_M\} = \emptyset,$$

there is a subsequence (which we do not bother to relabel) such that ϕ^Δ converges in $L^1(\mathcal{S} \times [0,T])$. Taking a countable sequence of intervals $\mathcal{S}_\nu$ satisfying (4.20) and

$$\bigcup_{\nu=1}^{\infty} \mathcal{S}_\nu = [0,L] \setminus \{\xi_1, \ldots, \xi_M\},$$

and employing a standard diagonal process we can extract a subsequence (which we again do not relabel) such that ϕ^Δ converges in $L^1(\Pi_T)$ and also a.e. in Π_T to some $\phi \in L^1(\Pi_T) \cap L^\infty(\Pi_T)$. That the limit ϕ is also in $BV_t(\Pi_T)$ is a consequence of the time continuity estimate (4.9). We have verified that the limit ϕ satisfies (4.5) of Definition 4.1.

That the limit ϕ satisfies the entropy inequality is a consequence of a Lax-Wendroff type calculation, which we omit since it is similar to the proof Lemma 4.1 of [37], see also the proof of of Theorem 3.1 of [16]. A proof of (4.6), i.e., that the initial values are assumed in the strong L^1 sense, can be found in [38], specifically, the proofs of Theorem 5.1 and Lemma B.1.

Finally, by the uniqueness portion of Theorem 4.1, the entire computed sequence ϕ^Δ (not just a subsequence) converges to ϕ in $L^1(\Pi_T)$ and boundedly a.e. in Π_T. □

5. NUMERICAL EXAMPLES

5.1. **Example 1: Scalar equation without spatially varying parameters.** To study the scalar scheme in the simplest possible setting, we apply Scheme 1 and the Lax-Friedrichs (LxF) flux

$$(5.1) \qquad h_{j+1/2}^{\mathrm{LxF}} := \frac{1}{2}\left(\phi_{j+1}v_{j+1} + \phi_j v_j\right) - \frac{q}{2\lambda}(\phi_{j+1} - \phi_j)$$

to the initial value problem

$$(5.2) \qquad \phi_t + \left(\phi(1-\phi)^\nu\right)_x = 0, \quad \phi_0(x) = \begin{cases} 0.85 & \text{if } |x| > 1, \\ 0.1 & \text{if } |x| < 1. \end{cases}$$

For the parameter q appearing in (5.1), we take $q = 1/2$ because this ensures that the resulting scheme satisfies the maximum principle (3.13) and TVD property (3.14). Plots (a) and (b) of Figure 1 show that for $\nu = 1$, both schemes give similar results. Plots (c) and (d) illustrate that for $\nu = 5$, the schemes based on (3.8) (both first-order and second-order versions, Schemes 1 and 10) give better resolution than the schemes based on the LxF flux. The solid line in all plots of Figure 1 is a reference solution, computed using Scheme 10, and the discretization parameters reduced by a factor of 8.

5.2. **Example 2: Scalar equation with spatially varying coefficients.** We next apply the variant of Scheme 1 that applies to conservation laws with discontinuous flux, namely Scheme 3, and Scheme 10 to scalar conservation laws with discontinuous flux of the form (2.2). The equation considered is

$$\phi_t + \left(v_{\max}(x)\phi(1 - \phi/\phi_{\max}(x))\right)_x = 0.$$

In Figures 2 (a) and (b) we use

$$(5.3) \qquad \phi_{\max} = 1, \quad \phi_0(x) = \begin{cases} 0.8 & \text{for } x < 0, \\ 0.1 & \text{for } x > 0, \end{cases} \quad v_{\max}(x) = \begin{cases} 1.0 & \text{for } x < 0, \\ 0.5 & \text{for } x > 0. \end{cases}$$

In Figures 2 (c) and (d) we set

$$(5.4) \qquad \phi_{\max}(x) = \begin{cases} 1.0 & \text{for } x < 0, \\ 0.5 & \text{for } x > 0, \end{cases} \quad \phi_0(x) = \begin{cases} 0.3 & \text{for } x < 0, \\ 0.7 & \text{for } x > 0, \end{cases} \quad v_{\max} = 1.$$

The solid line visible in all plots is a reference solution, computed using Scheme 10, and the discretization parameters reduced by a factor of 16.

In each case, the new scheme (Scheme 3 or 10) gives better resolution than the corresponding scheme based on the LxF flux. Note that there is some overshoot visible in plots (a) and (b). This overshoot originates at the location of the jump in $v_{\max}$, and then propagates as a traveling wave (a bump). As the
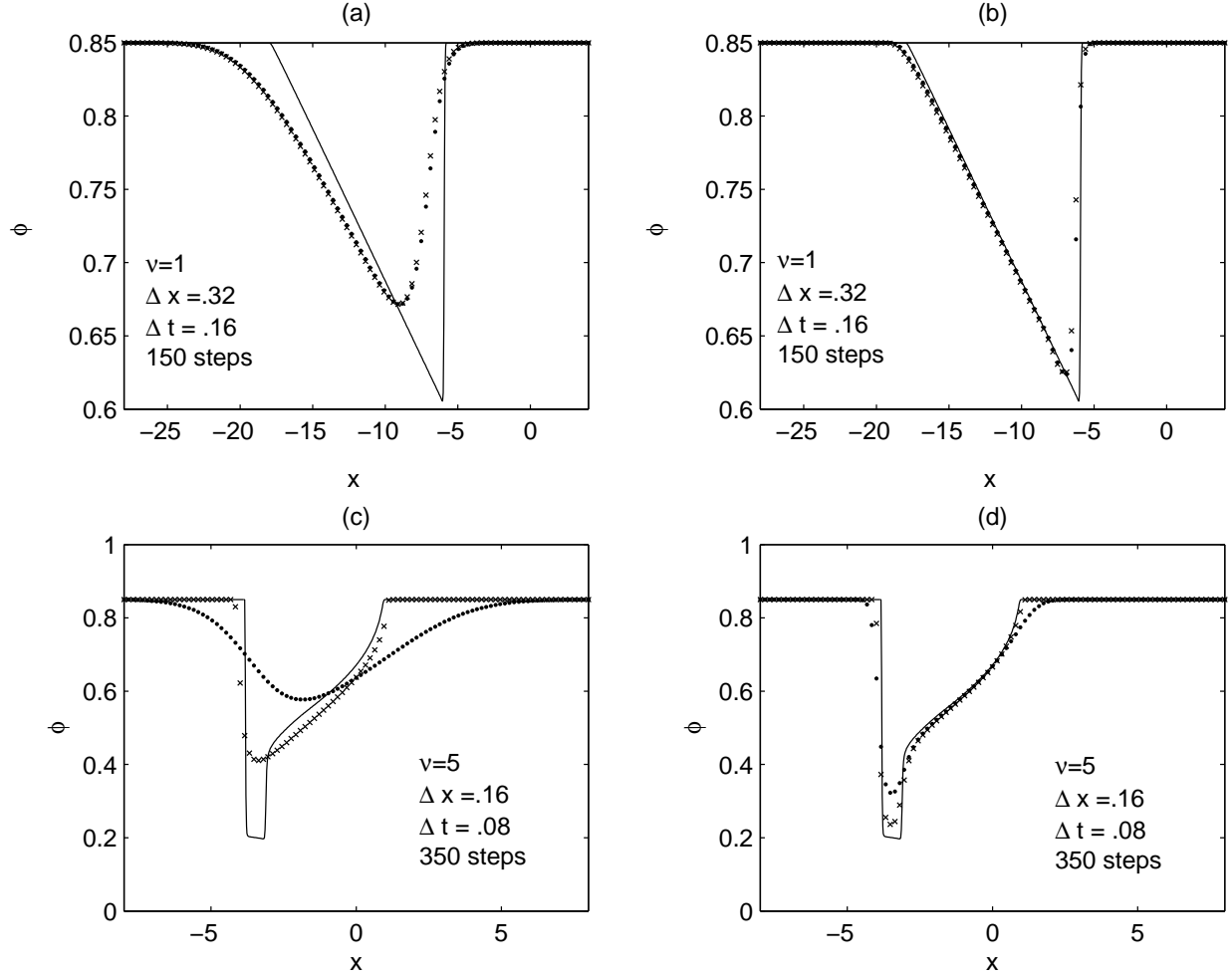
FIGURE 1. Example 1 (scalar case, problem (5.2)): Scheme 1 ($\times$) (a, c), Scheme 10 ($\times$) (b, d) and LxF flux ($\cdot$). Plot (a): first-order schemes, $\nu = 1$. Plot (b): second-order schemes, $\nu = 1$. Plot (c): first-order schemes, $\nu = 5$. Plot (d): second-order schemes, $\nu = 5$. The solid line is the reference solution.

mesh size approaches zero, the magnitude and width of the bump approaches zero. Clearly, this non-physical feature is more pronounced for the LxF scheme.

5.3. **Example 3: Clarifier-thickener model.** We now adapt our scheme to the clarifier-thickener model with constant cross-sectional area studied in [16], specifically Example 2 of that paper. In this case the conservation law is of the form

$$(5.5) \qquad \phi_t + \big(\phi[a(x)\mathcal{S}(\phi) + c(x)] + b(x)\big)_x = 0, \quad x \in \mathbb{R}, \quad t > 0,$$

where $\mathcal{S}(\phi) = \phi_\infty(1 - \phi)^2$ and

$$a(x) = \begin{cases} 1 & \text{for } x \in (-1, 1), \\ 0 & \text{for } x \notin (-1, 1), \end{cases} \quad b(x) = \begin{cases} -q_\mathrm{L}\phi_\mathrm{F} & \text{for } x < 0, \\ -q_\mathrm{R}\phi_\mathrm{F} & \text{for } x > 0, \end{cases} \quad c(x) = \begin{cases} q_\mathrm{L} & \text{for } x < 0, \\ q_\mathrm{R} & \text{for } x > 0. \end{cases}$$

Except for the term $b(x)$ which we discretize separately, this problem fits into the framework of (3.1) with $N = 1$, and the velocity $v(\phi, x) = a(x)\mathcal{S}(\phi) + c(x)$, which may assume either sign. Consequently, and
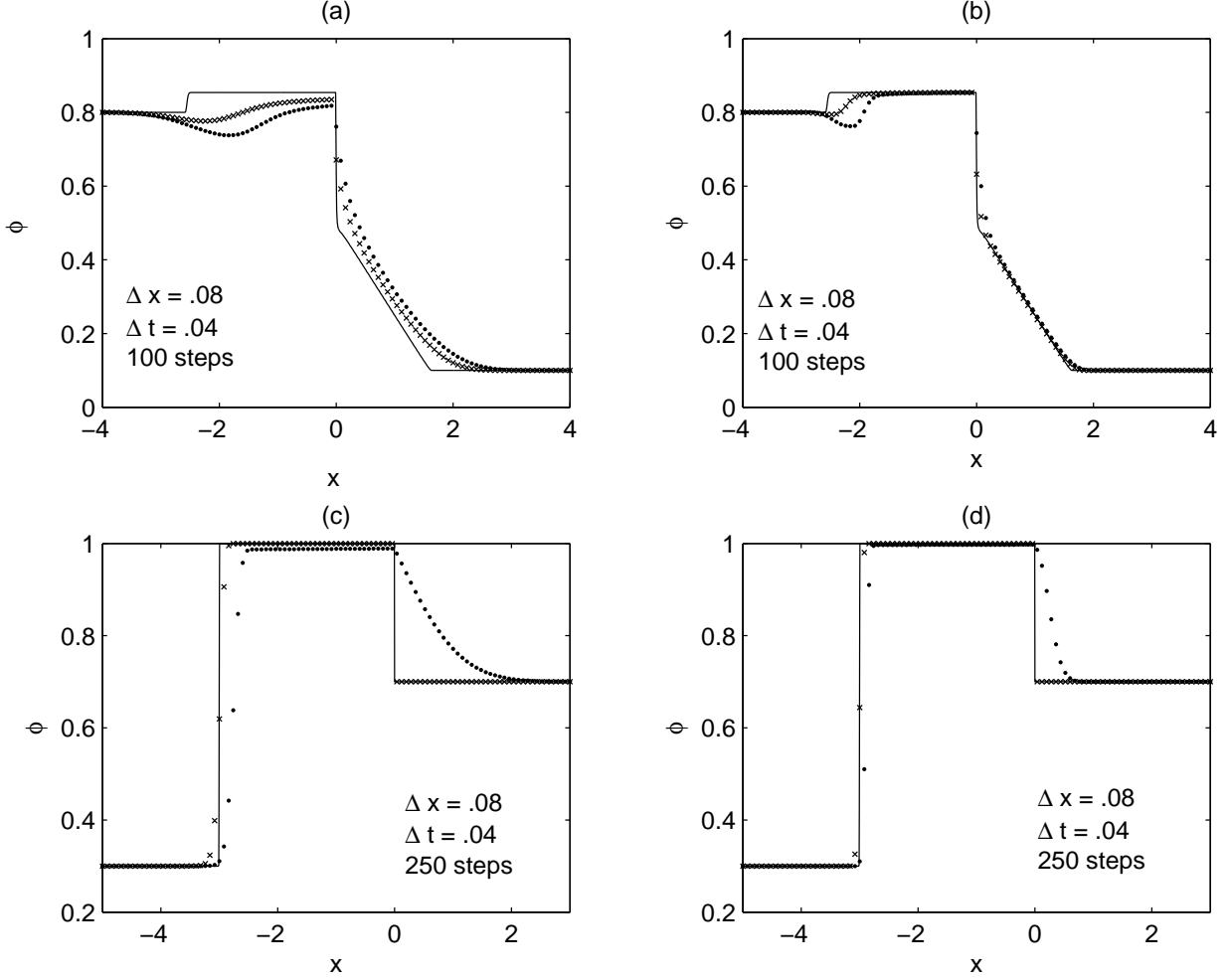
FIGURE 2. Example 2 (scalar case with discontinuous flux, see (5.2)): Scheme 3 ($\times$) (a, c), Scheme 10 ($\times$) (b, d) and LxF flux ($\cdot$). Plot (a): coefficients (5.3), first-order schemes. Plot (b): coefficients (5.3), second-order schemes. Plot (c): coefficients (5.4), first-order schemes. Plot (d): coefficients (5.4), second-order schemes. The solid line is the reference solution.

following (3.9), the appropriate first-order scheme is Scheme 2, whose numerical flux is defined by

$$(5.6) \qquad h_{j+1/2} = \phi_j \max\{0, v_{j+1}\} + \phi_{j+1} \min\{0, v_{j+1}\} + b_{j+1}, \quad v_j := a_j \mathcal{S}(\phi_j) + c_j.$$

Note that we use b_{j+1}, as opposed to b_j (or some average of the two values) for the first-order version of the scheme. Indeed, this biased discretization of the parameter b can be motivated by the requirement that if $\mathcal{S} \equiv 0$, then $\phi \equiv \phi_F$ should be a stationary solution of (5.5).

For the second-order version of the scheme, we discretize $\boldsymbol{\gamma}(x) := (a(x), c(x))$ as in (3.39), and and continue to use b_{j+1} in (5.6); this discretization of $b(x)$ preserves the steady solution $\phi \equiv \phi_F$ if $\mathcal{S} \equiv 0$. We use the Van Leer limiter (3.41), so the scheme in question is Scheme 10.

For our experiments, we used the same parameters as for Example 2 of [16], namely $q_L = -1$, $q_R = 0.6$, $\phi_F = 0.8$ and $\phi_\infty = 27/4$. For discretization parameters, we used $\Delta x = 5 \times 10^{-3}$, $\Delta t = 3.125 \times 10^{-4}$, implying $\lambda = 1/16$; this value of λ was chosen to agree with Example 2 of [16]. We started with initial data $\phi_0 \equiv 0$. Plot (a) of Figure 3 shows the solution at $t = 1$, and plot (b) shows the solution at $t = 3$. These
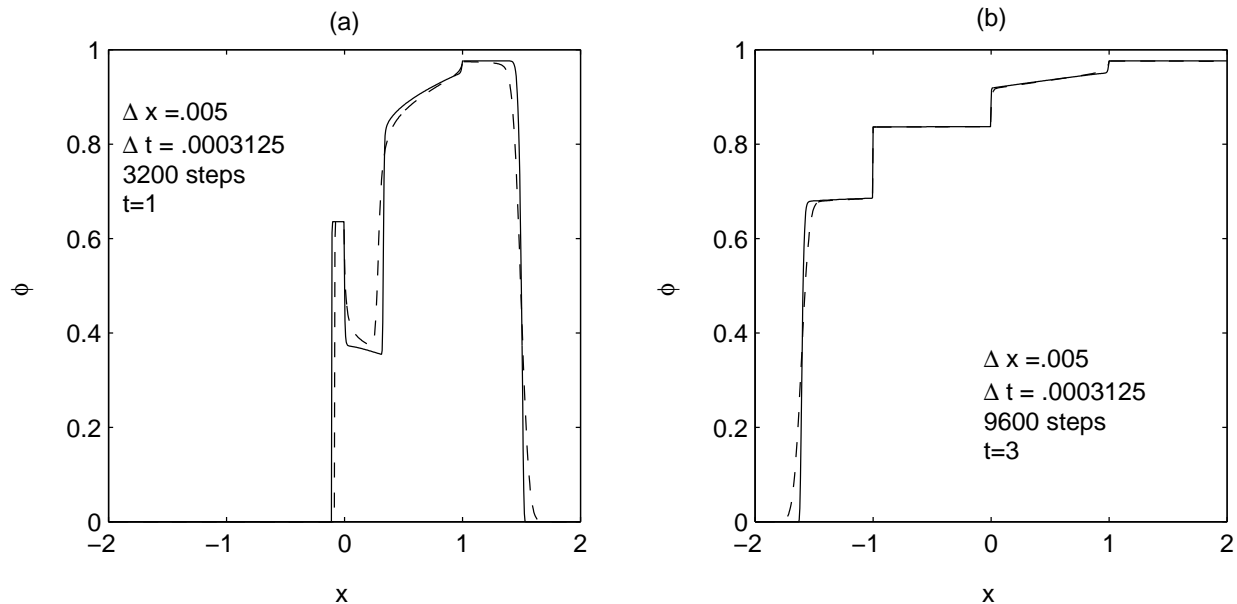
FIGURE 3. Example 3 (clarifier-thickener model (5.5)): (first-order) Scheme 2 (dashed line) and second-order Scheme 10 (solid line). Plot (a) shows $t = 1$, plot (b) shows $t = 3$.

approximations are in good agreement with the solutions obtained in Example 2 of [16]. Scheme 2 provides a somewhat less accurate solution than the one provided by the Engquist-Osher scheme proposed in [16]. However, Scheme 2 is much easier to code, and at least with our implementation, runs significantly faster.

5.4. **Example 4: Multi-species traffic model.** Zhang et al. [4] present numerical simulations of a traffic flow model with $N = 9$ species (classes) of vehicles with the maximum velocities $v_{\max}^i = (52.5 + i \cdot 7.5)\,\mathrm{km/h}$, $i = 1, \ldots, 9$. We consider here Case 2 simulated in [4], where the function $V(\phi) = \exp(-(\phi/\phi_*)^2/2)$ with the parameter $\phi_* = 50\,\mathrm{cars/km}$ is used. This case, which forms our Example 4, consists of the evolution of an isolated initial traffic "platoon" given by $\Phi^0(x) = p(x)0.04\phi^0(1, 2, 3, 4, 5, 4, 3, 2, 1)^{\mathrm{T}}$, where

$$p(x) := \begin{cases} 10x & \text{for } 0 < x \leq 0.1, \\ 1 & \text{for } 0.1 < x \leq 0.9, \\ -10(x - 1) & \text{for } 0.9 < x \leq 1, \\ 0 & \text{otherwise} \end{cases}$$

is the platoon "shape function", where x denotes distance measured in kilometers and $\phi^0 = 120\,\mathrm{cars/km}$. We here use this example to compare the performance of Scheme 4, which is the first-order version of the scheme that applies to systems with non-negative velocities only, with the standard first-order LxF scheme; and that of Scheme 9, which is the second-order version of Scheme 4 generated by spatial MUSCL extrapolation in combination with a second-order RK type discretization, with that of a second-order version of the LxF scheme generated by the analogous MUSCL/RK "upgrades". The reference solution was calculated using Scheme 9 with the discretization parameters $\Delta x = 1/480\,\mathrm{km}$. The reference solution and all numerical solutions of this example have been calculated with $\lambda = 1/240\,\mathrm{h/km}$.

In Examples 4 and 6, we record an approximate L^1 error defined with respect to the reference solution, to evaluate the performance of some of the new schemes. We introduce two types of L^1 error, denoted e_1
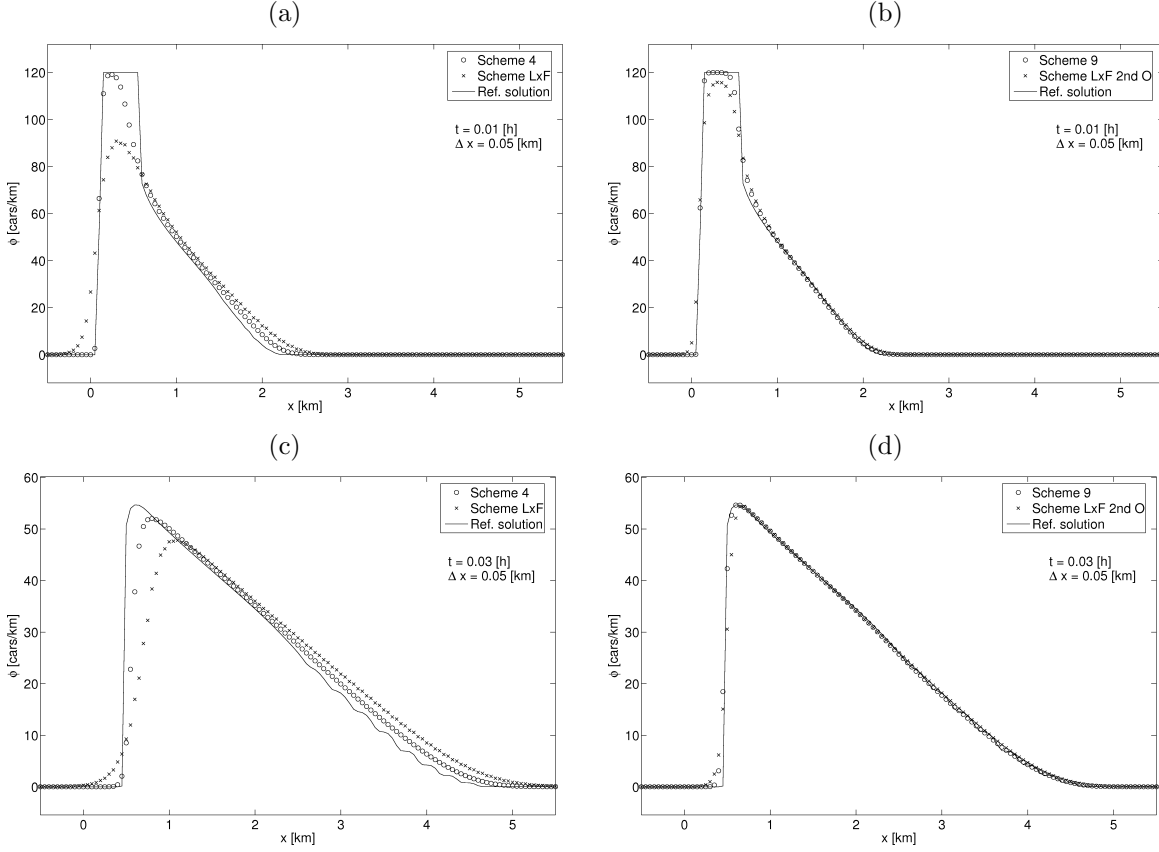
FIGURE 4. Example 4 (traffic model, $N = 9$): simulated total car density. Plots (a, c): first-order schemes (LxF and Scheme 4). Plots (b, d): second-order schemes (LxF MM/RK and Scheme 9). Plots (a, b) show $t = 0.01\,\mathrm{h}$, and plots (c, d) show $t = 0.03\,\mathrm{h}$.

and e_2, which are defined by

$$e_1 := \widetilde{\Delta x} \sum_{i=M_{\mathrm{L}}}^{M_{\mathrm{R}}} \sum_{j=1}^{m} \sum_{k=1}^{N} \big|\tilde{\phi}^n_{k,m(i-1)+j} - \phi^n_{k,i}\big|, \quad e_2 := \widetilde{\Delta x} \sum_{i=M_{\mathrm{L}}}^{M_{\mathrm{R}}} \sum_{j=1}^{m} \bigg|\sum_{k=1}^{N} \big(\tilde{\phi}^n_{k,m(i-1)+j} - \phi^n_{k,i}\big)\bigg|,$$

where $\tilde{\phi}^n_{k,\tilde{l}}$ and $\phi^n_{k,l}$ are the reference solution at $x = x_{\tilde{l}}$ and the approximate solution at $x = x_l$, respectively, both for species k at $t = t_n$; m is the value of Δx of the approximate solution divided by that of the reference solution; M_{L} and M_{R} are the indices of the positions between which we calculate the errors of the numerical approximation; and $\widetilde{\Delta x}$ is the spatial discretization parameter of the reference solution.

For Example 4, Figure 4 shows the simulated total car density at two times produced by the LxF scheme, Scheme 4, the second-order version of the LxF scheme using the minmod limiter, and Scheme 9, while Table 1 displays the approximate L^1 errors for this example, measured over the interval $[-1\,\mathrm{km}, 6\,\mathrm{km}]$. Both Figure 4 and Table 1 indicate the superiority of Scheme 4 over the LxF scheme, and of Scheme 9 over the second-order MM/RK upgrade of the LxF scheme, respectively.

5.5. **Example 5: Multiclass traffic model with spatially varying** $\phi_{\max}$**.** As an example where the flux has a spatially varying parameter, we also present two simulations (Examples 5.1 and 5.2) that can be compared with numerical results by Zhang et al. [6]. The model is the multi-class traffic model of Section 2.1, whose flux is given by (2.4). Both examples are Riemann problems, and $N = 3$. The (normalized [6])

$\mathcal{J}+1$	$t = 0.01\,\mathrm{h}$				$t = 0.03\,\mathrm{h}$			
$= L/\Delta x$	e_1 [cars]	Conv. rate	e_2 [cars]	Conv. rate	e_1 [cars]	Conv. rate	e_2 [cars]	Conv. rate
Scheme LxF								
100	35.121		34.660		29.365		27.091	
200	21.885	0.682	21.317	0.701	19.163	0.616	15.372	0.818
300	16.298	0.727	15.657	0.761	15.232	0.566	10.702	0.893
400	13.187	0.736	12.486	0.787	13.110	0.522	8.176	0.936
600	9.830	0.725	9.034	0.798	10.830	0.471	5.536	0.962
Scheme 4								
100	15.634		15.197		17.798		14.137	
200	9.193	0.766	8.639	0.815	11.730	0.601	7.492	0.916
300	6.877	0.716	6.197	0.819	9.399	0.546	5.096	0.950
400	5.614	0.705	4.859	0.845	8.095	0.519	3.866	0.960
600	4.229	0.699	3.431	0.858	6.619	0.496	2.623	0.957
Scheme LxF MM/RK								
100	14.649		13.589		11.608		5.941	
200	7.880	0.895	6.852	0.988	8.405	0.466	2.563	1.213
300	5.602	0.842	4.596	0.985	7.257	0.362	1.741	0.954
400	4.505	0.757	3.457	0.990	6.476	0.396	1.414	0.722
600	3.376	0.711	2.263	1.044	5.450	0.425	1.052	0.730
Scheme 9								
100	8.619		7.786		8.509		3.570	
200	4.749	0.860	3.857	1.014	5.986	0.508	1.830	0.964
300	3.410	0.817	2.534	1.036	4.845	0.521	1.310	0.824
400	2.700	0.811	1.853	1.087	4.116	0.567	1.016	0.884
600	1.885	0.887	1.151	1.175	3.114	0.688	0.680	0.991

TABLE 1. Example 4: approximate L^1 errors.

maximum velocities are constant: $v_{\max}^1 = 0.50$, $v_{\max}^2 = 0.75$ and $v_{\max}^3 = 1.00$. We use the second-order scheme of Section 3.5 with the minmod limiter (3.40) (Scheme 9). The mesh size for both problems is $\Delta x = 6.25 \times 10^{-4}$, $\Delta t = 1.25 \times 10^{-4}$. We march the solution forward in time for 8000 steps, arriving at $t = 1$. The initial data Φ^0 and maximum density $\phi_{\max}$ are constant except for a jump at $x_0 \in (0,1)$,

$$\phi_{\max}(x) = \begin{cases} 3 & \text{for } x < x_0, \\ 1 & \text{for } x > x_0, \end{cases} \quad \Phi^0(x) = \begin{cases} \Phi_{\mathrm{L}}^0 & \text{for } x < x_0, \\ \Phi_{\mathrm{R}}^0 & \text{for } x > x_0. \end{cases}$$

For Examples 5.1 and 5.2, we choose $x_0 = 0.5$, $\Phi_{\mathrm{L}}^0 = (0.6, 0.3, 0.9)^{\mathrm{T}}$ and $\Phi_{\mathrm{R}}^0 = (0.1, 0.0, 0.5)^{\mathrm{T}}$, and $x_0 = 0.3$, $\Phi_{\mathrm{L}}^0 = (0.6, 0.45, 0.15)^{\mathrm{T}}$ and $\Phi_{\mathrm{R}}^0 = (0.05, 0.15, 0.2)^{\mathrm{T}}$, respectively. As shown in Figure 5, for both problems, the various waves are well resolved, and there is good agreement with the results obtained by Zhang et al. in [6] (see Figures 4 and 7 of that paper).

5.6. **Example 6: Settling of a bidisperse suspension of equal-density spheres.** In this example, the parameters are $N = 2$, $\varrho_1 = \varrho_2 = \varrho_{\mathrm{s}} = 2790\,\mathrm{kg/m^3}$, $d_1 = 4.96 \times 10^{-4}\,\mathrm{m}$, $d_2 = 1.25 \times 10^{-4}\,\mathrm{m}$, $\varrho_{\mathrm{f}} = 1208\,\mathrm{kg/m^3}$ and $\mu_{\mathrm{f}} = 0.02416\,\mathrm{Pa\,s}$. Here, we have $\delta_1 = 1$ and $\delta_2 = d_2^2/d_1^2 = 0.06351213$. For this mixture, we select the phase space $\mathcal{D}_{0.68}$ [23] and the function $V(\phi)$ given by (2.6) with the exponent $n = 4.7$; all these parameters correspond to experimental data by Schneider et al. [55]. As in [55], we consider an initially homogeneous suspension with $\Phi^0 = (\phi_1^0, \phi_2^0)^{\mathrm{T}} = (0.2, 0.05)$ in a vessel of height $L = 0.3\,\mathrm{m}$.

The reference solution was calculated using the Scheme 10 with the discretization parameter $\Delta x = 1/8000\,\mathrm{m}$. For the reference solution and all other computations of this example, we use $\lambda = 56.95\,\mathrm{s/m}$.
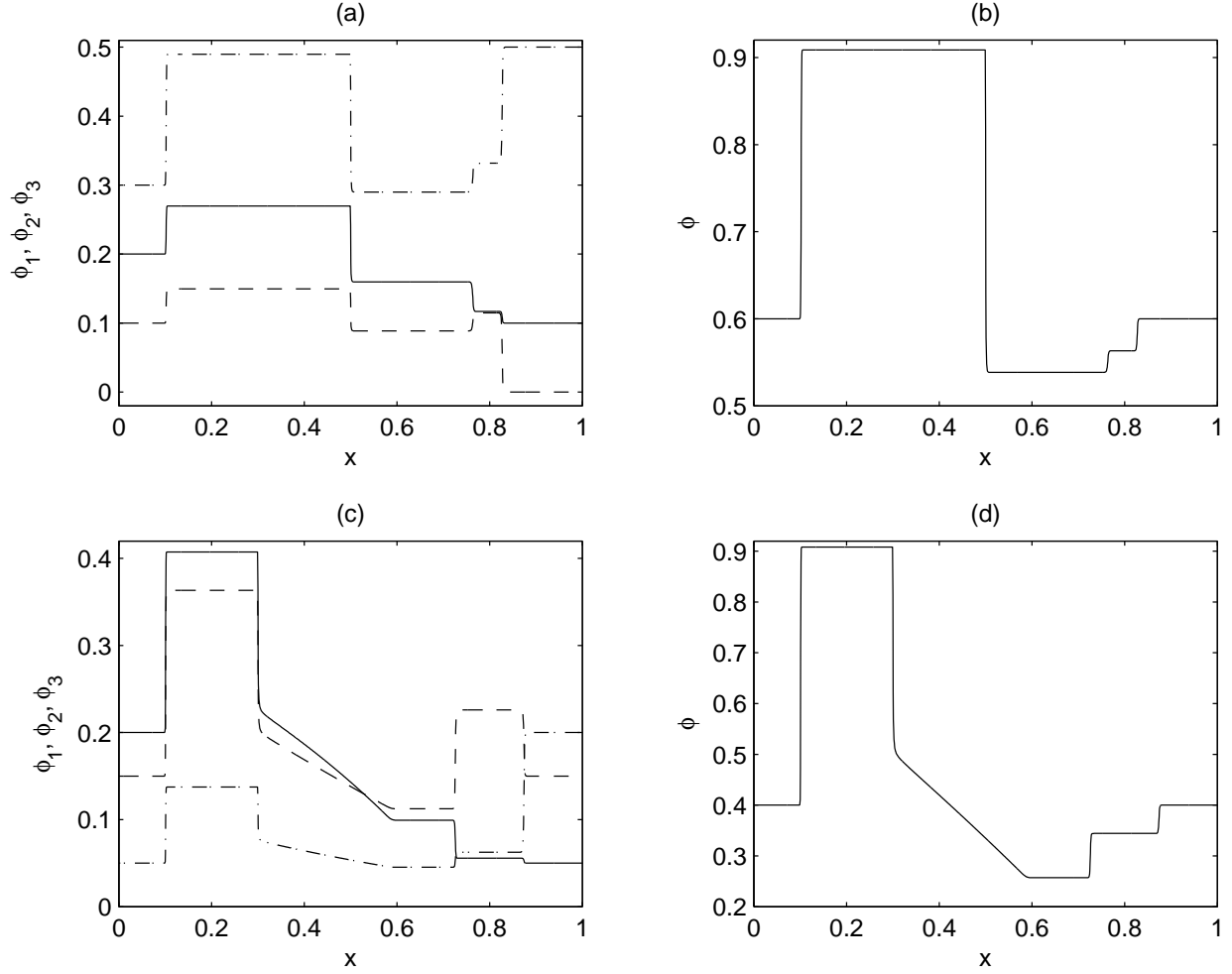
FIGURE 5. Examples 5.1 (a, b) and 5.2 (c, d) (traffic model with spatially varying $\phi_{\max}$, $N = 3$): plots (a, c) show $\phi_1/\phi_{\max}$ (solid line), $\phi_2/\phi_{\max}$ (dashed line), $\phi_3/\phi_{\max}$ (dash-dotted line). Plots (b, d) show $(\phi_1 + \phi_2 + \phi_3)/\phi_{\max}$. Solutions are obtained by Scheme 9.

For Example 6, Figure 6 shows the numerical solution of the total solids concentration for $t = 60\,\mathrm{s}$ and $t = 240\,\mathrm{s}$, produced by the first-order LxF scheme, Schemes 6 and 8, the second-order version of the LxF scheme involving the Van Leer limiter function, Scheme 8 with the Van Leer limiter function, and Scheme 10, while Table 2 displays the approximate L^1 errors for this example, measured over the interval $[0\,\mathrm{m}, 0.3\,\mathrm{m}]$. (Again, all second-order schemes utilize RK time stepping.)

It is clear from Figure 6 that Schemes 6 and 8 and their second order versions are less dissipative than their counterparts based on the LxF flux. In plots (c) and (d), there is a spurious "kink" and a small overshoot in the solution created by Schemes 6 and 10. These artifacts are diminished by using instead the more viscous Scheme 8, and its second order version. In the reference solution, which is computed using a very fine mesh, these features are not visible at all. Table 2 corroborates what we see in the plots, specifically, smaller errors and faster rates of convergence for Schemes 6 and 8 and their second order versions than the LxF based schemes. It is interesting that Scheme 6, which is formally first order accurate, has smaller errors at $t = 240\,\mathrm{s}$ than the formally second order accurate version of the LxF scheme.
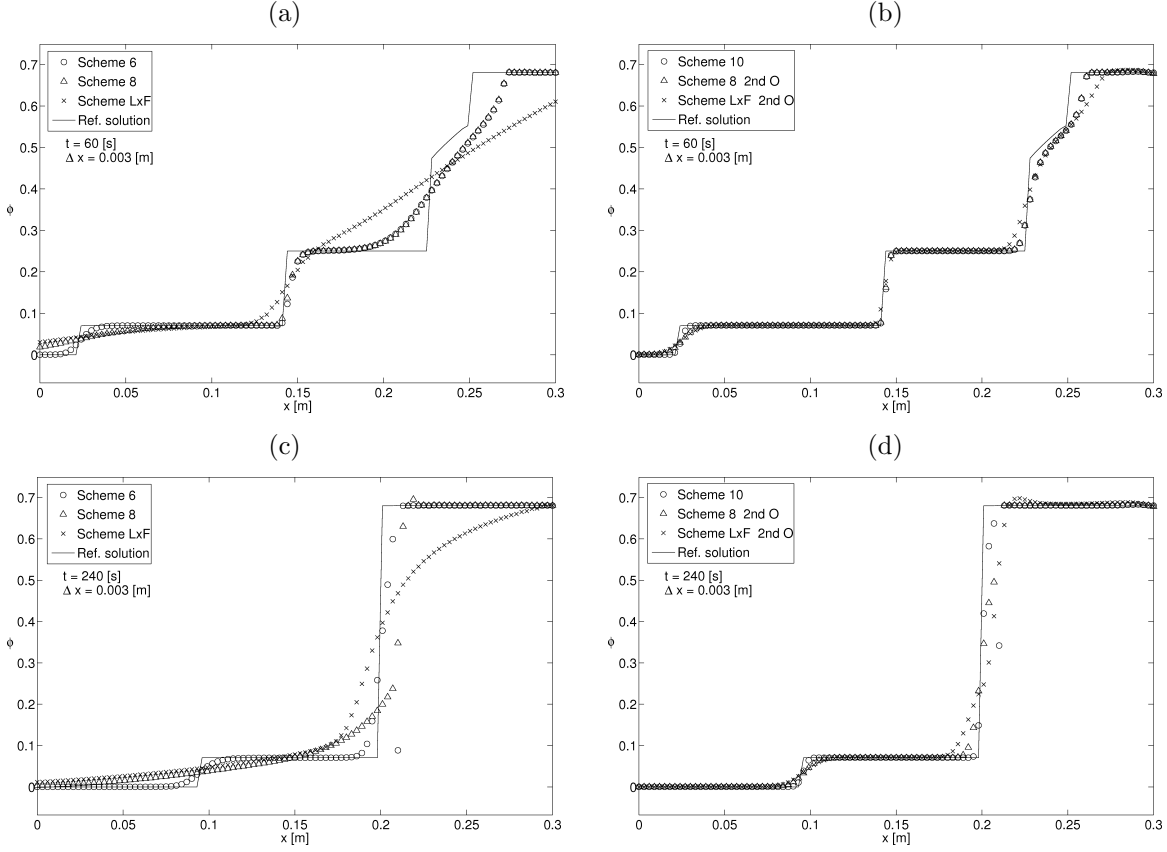
FIGURE 6. Example 6 (settling of a suspension of equal-density spheres, $N = 2$): simulated total solids concentration. Plots (a, c): first-order schemes (LxF, Schemes 68 and 8). Plots (b, d): second-order schemes (LxF VL/RK, Scheme 8 VL/RK and Scheme 9). Plots (a, b) show solutions at $t = 60$ s, and plots (c, d) show solutions at $t = 240$ s.

5.7. **Example 7: Settling of a suspension with particles of 11 different sizes.** To illustrate that the new method handles systems with a large number of particle species, we consider a suspension of equal-density particles of $N = 11$ different sizes. The parameters and initial concentrations of these size classes are displayed in Table 3. This size distribution was determined by Tory et al. [9] as a discrete approximation for a suspension of closely-sized spherical particles with continuously, roughly normally distributed particle sizes [70]. Following [70], we consider a settling column of height $L = 0.935$ m. The hindered settling factor found suitable is (2.6) with $n = 4.65$ and $\phi_{\max} = 0.641$. According to [70], a single sphere with diameter 6.694×10^{-5} m has a Stokes velocity of $\tilde{v}_\infty = 0.00392$ m/s, so we here use (2.9) with $v_\infty = (8.769/6.694)^2 \tilde{v}_\infty = 0.00673$ m/s. We calculate the numerical solution at the times $t = t_1 = 247.77$ s, $t = t_2 = 412.94$ s and $t_3 = 578.15$ s, using Scheme 10 with the discretization parameters $\Delta x = 9.13 \times 10^{-4}$ m $= L/1024$ and $\Delta t = \lambda \Delta x$, where $\lambda = 74.29$ s/m. The values of Δx and t_1, t_2 and t_3 have been chosen such that results can be compared with the numerical solution of the same example by the multiresolution WENO scheme done by Bürger and Kozakevicius [29].

Figures 7, 8 and 9 show the numerical solutions of each species concentration and the total solids concentration for $t = 247.77$ s, $t = 412.94$ s, and $t = 578.15$ s, respectively, over intervals where the solutions are different from zero. By comparing these figures with Figures 18, 19, and 20 of [29], it is clear that Scheme 10 captures the same solution as the multiresolution scheme of that paper.

$\mathcal{J}+1$ $=L/\Delta x$	$t=60\,\mathrm{s}$				$t=240\,\mathrm{s}$			
	e_1 10^{-3}	Conv. rate	e_2 10^{-3}	Conv. rate	e_1 10^{-3}	Conv. rate	e_2 10^{-3}	Conv. rate
	LxF scheme							
100	19.617		18.381		26.033		18.410	
200	14.294	0.457	13.525	0.443	18.788	0.471	11.702	0.654
300	11.576	0.520	10.978	0.515	16.267	0.355	9.572	0.496
400	9.926	0.535	9.366	0.552	14.916	0.301	8.479	0.422
600	7.959	0.545	7.430	0.571	13.306	0.282	7.230	0.393
	Scheme 8							
100	11.033		10.004		15.499		12.348	
200	6.999	0.657	6.293	0.669	11.397	0.444	9.002	0.456
300	5.370	0.654	4.828	0.654	9.433	0.467	7.134	0.574
400	4.447	0.655	3.992	0.660	8.095	0.532	6.097	0.546
600	3.419	0.649	3.065	0.652	6.595	0.505	4.852	0.563
	Scheme 6							
100	9.965		9.032		10.913		7.163	
200	6.104	0.707	5.501	0.715	7.201	0.600	3.534	1.019
300	4.606	0.694	4.142	0.700	5.000	0.900	2.583	0.774
400	3.776	0.691	3.380	0.706	3.995	0.780	2.082	0.750
600	2.867	0.679	2.555	0.690	3.089	0.635	1.447	0.897
	Scheme LxF VL/RK							
100	7.134		6.269		13.180		8.510	
200	3.741	0.931	3.281	0.934	8.717	0.596	5.130	0.730
300	2.479	1.015	2.170	1.020	6.849	0.595	3.786	0.749
400	1.861	0.996	1.626	1.002	5.719	0.627	3.047	0.756
600	1.196	1.091	1.046	1.088	4.384	0.656	2.182	0.824
	Scheme 8 VL/RK							
100	5.900		5.203		10.955		6.103	
200	2.947	1.001	2.599	1.001	5.967	0.876	3.276	0.897
300	1.920	1.057	1.692	1.059	3.992	0.992	2.185	0.999
400	1.413	1.066	1.246	1.062	3.095	0.884	1.778	0.716
600	0.890	1.141	0.785	1.140	1.862	1.254	1.033	1.339
	Scheme 10							
100	5.620		5.005		8.648		5.125	
200	2.725	1.045	2.427	1.044	4.183	1.048	2.537	1.015
300	1.742	1.104	1.554	1.099	2.584	1.188	1.635	1.083
400	1.262	1.119	1.125	1.122	1.849	1.164	1.248	0.939
600	0.762	1.245	0.680	1.242	1.182	1.102	0.776	1.173

TABLE 2. Example 6: approximate L^1 errors.

In all figures we notice that larger species settle first and fill the lower layers of the vessel. In Figure 8 we can see spurious tips in the solutions of the species 4 to 9, which do not appear in Figures 7 and 9. There are also peaks in the simulated total concentration in Figures 8 and 9. It is clear that this does not have physical sense and therefore is a numerical artefact.

5.8. **Example 8: Oil-in-water dispersion model: Creaming of a dispersion with 10 different droplet sizes.** We consider the settling of a dispersion of droplets of diesel oil in water. We utilize the droplet size distribution with $N = 10$ given by Figure 2 of Das and Biswas [71], a histogram of relative

i	$d_i\,[10^{-5}\,\mathrm{m}]$	δ_i	ϕ_i^0
1	8.769	1.0000	0.000435
2	8.345	0.9056	0.003747
3	7.921	0.8159	0.014420
4	7.497	0.7309	0.032603
5	7.073	0.6506	0.047912
6	6.649	0.5749	0.047762
7	6.225	0.5039	0.032663
8	5.801	0.4376	0.015104
9	5.377	0.3760	0.004511
10	4.953	0.3190	0.000783
11	4.529	0.2668	0.000060

TABLE 3. Example 7: Parameters for the settling of a suspension with $N = 11$ particle sizes.
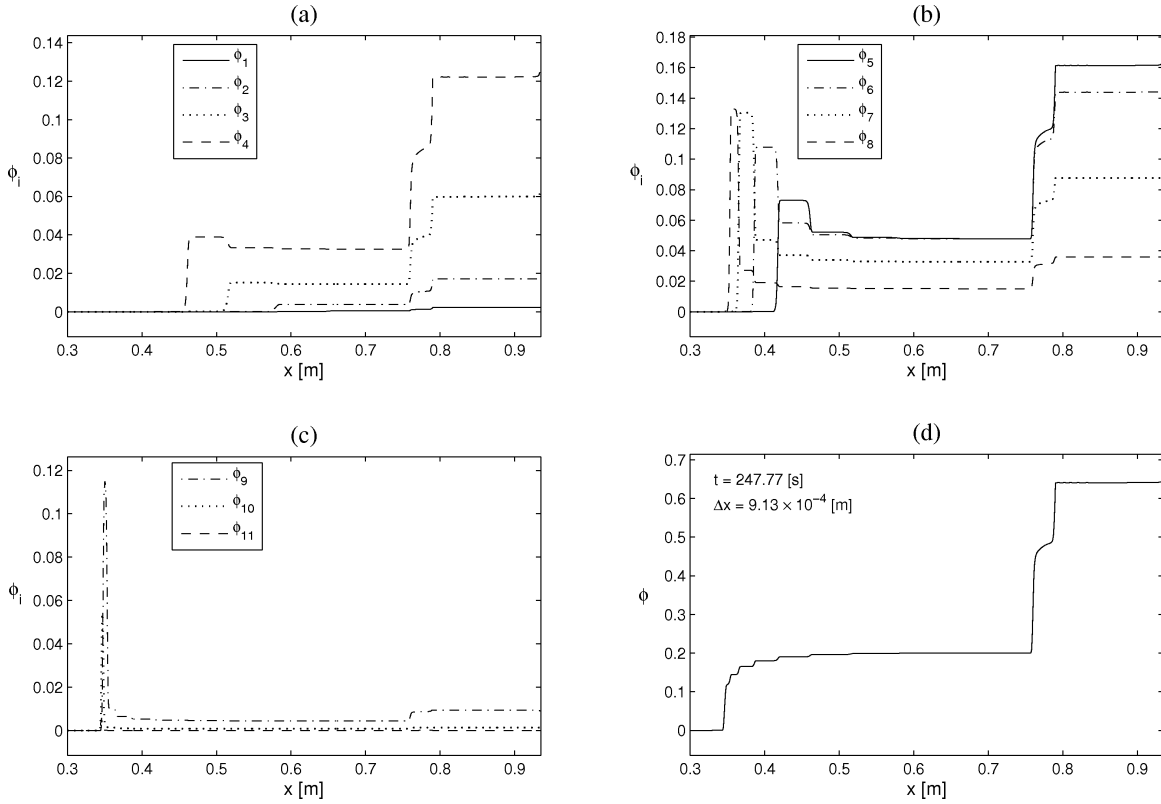
FIGURE 7. Example 7 (settling of a suspension with particles of $N = 11$ different sizes): solids concentrations at $t = 247.77\,\mathrm{s}$ simulated by Scheme 10.

frequencies, which is converted into the initial vector Φ^0 in Table 4. We use here the viscosity function $\mu_\mathrm{d}(\Phi) = \mu_\mathrm{d}(\phi) = \mu_\mathrm{f}(1 - \phi/\phi_\mathrm{max})^{-2}$, and consider the creaming of the mixture characterized by Table 4 in three different vessels of height $L = 1\,\mathrm{m}$ and with the bottom located in $x = 0$: Vessel 1 (Example 8.1), a settling column of unit cross-sectional area, Vessel 2 (Example 8.2), which is defined by the cross-sectional
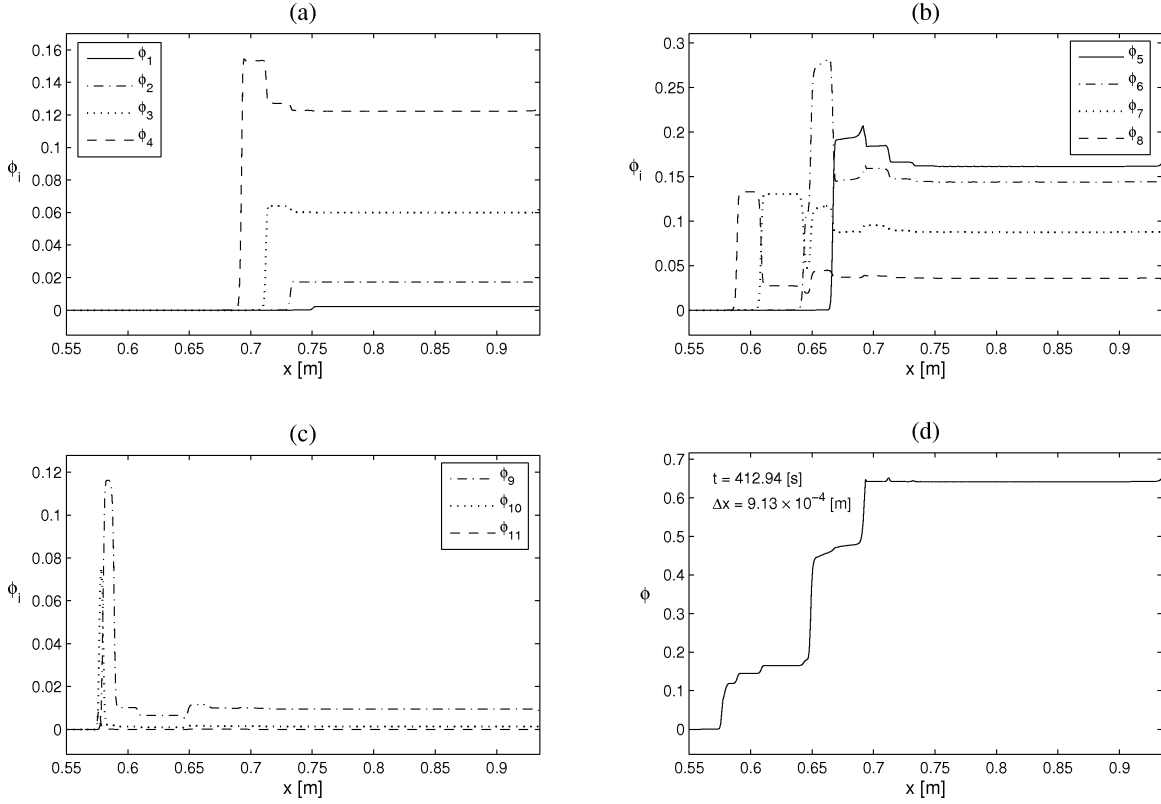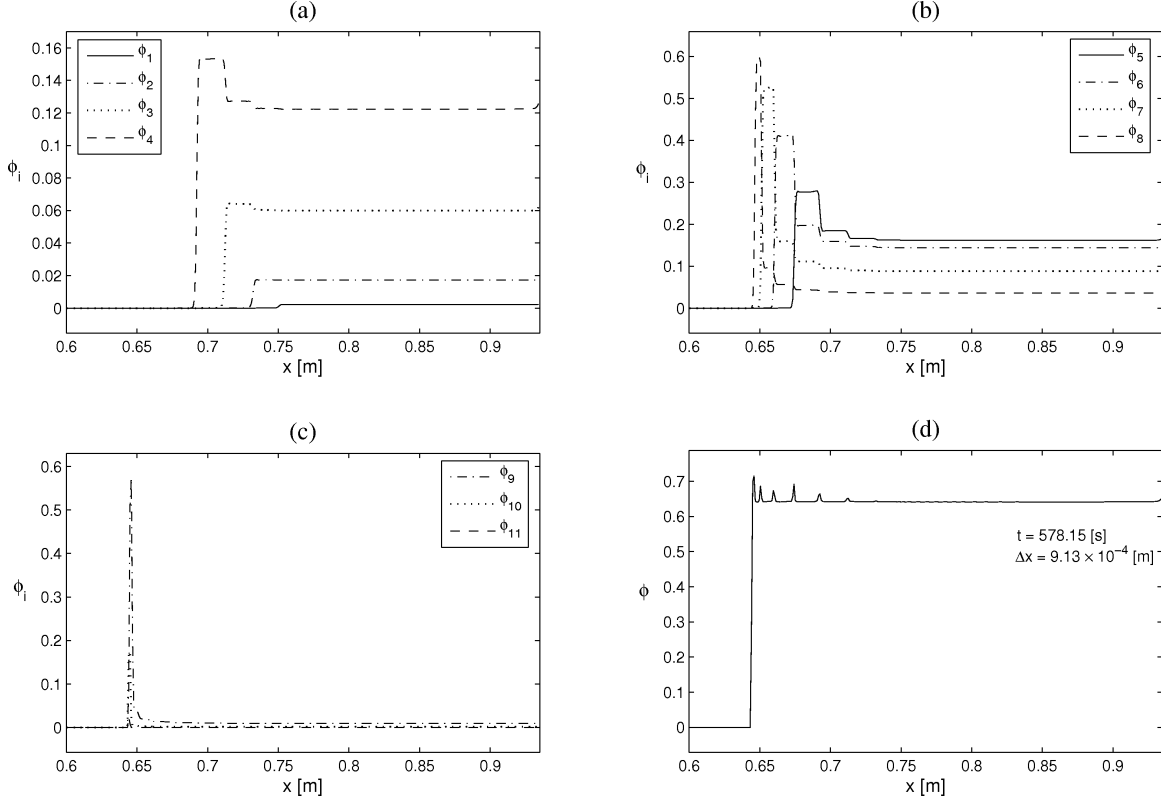
FIGURE 8. Example 7 (settling of a suspension with particles of $N = 11$ different sizes): solids concentrations at $t = 412.94\,\mathrm{s}$ simulated by Scheme 10.

i	$D_i\,[10^{-6}\,\mathrm{m}]$	$\mathcal{V}_i\,[10^{-18}\,\mathrm{m}^3]$	θ_i	ϕ_i^0/ϕ^0	ϕ_i^0
1	5	65.4	0.019	$6.654{\times}10^{-5}$	$3.327{\times}10^{-6}$
2	10	523.6	0.050	$1.401{\times}10^{-3}$	$7.004{\times}10^{-5}$
3	15	1767.1	0.047	$4.444{\times}10^{-3}$	$2.222{\times}10^{-4}$
4	20	4188.8	0.081	$1.815{\times}10^{-2}$	$9.077{\times}10^{-4}$
5	25	8181.2	0.148	$6.479{\times}10^{-2}$	$3.239{\times}10^{-3}$
6	30	14137.2	0.207	$1.566{\times}10^{-1}$	$7.829{\times}10^{-3}$
7	35	22449.3	0.202	$2.426{\times}10^{-1}$	$1.213{\times}10^{-2}$
8	40	33510.3	0.169	$3.030{\times}10^{-1}$	$1.515{\times}10^{-2}$
9	45	47712.9	0.064	$1.634{\times}10^{-1}$	$8.169{\times}10^{-3}$
10	50	65449.8	0.013	$4.553{\times}10^{-2}$	$2.276{\times}10^{-3}$

TABLE 4. Example 8: Droplet sizes and initial volume fractions for a dispersion of diesel oil in water according to [71].

area function

$$S_2(x) = \begin{cases} 0.0025\,\mathrm{m}^2 & \text{for } 0\,\mathrm{m} \le x \le 0.5\,\mathrm{m}, \\ 0.01\,\mathrm{m}^2 & \text{for } 0.5\,\mathrm{m} < x \le 1.0\,\mathrm{m}, \end{cases}$$

FIGURE 9. Example 7 (settling of a suspension with particles of $N = 11$ different sizes): solids concentrations at $t = 578.15\,$s simulated by Scheme 10.

and Vessel 3 (Example 8.3), which is just Vessel 2 turned "upside-down", and is characterized by the cross-sectional area function $S_3(x) := S_2(1.0\,\text{m} - x)$. Thus, in Examples 8.2 and 8.3, we have a system of conservation laws whose flux depends discontinuously on x. Namely, we have the initial value problem

$$S(x)\partial_t \phi_i + \partial_x f_i(S(x), \Phi) = 0, \quad (x, t) \in (0, L) \times (0, T) =: \Pi_T, \quad i = 1, \dots, N,$$

$$f_i(S(x), \Phi) = S(x)\phi_i v_i(\Phi), \quad \Phi(x, 0) = \Phi^0(x), \quad x \in (0, L),$$

which is supplemented by the zero-flux boundary conditions $f_i(S(0), \Phi) = f_i(S(L), \Phi) = 0$ for $i = 1, \dots, N$, where the cross-sectional area function S equals S_2 and S_3 for Vessels 2 and 3, respectively.

For Examples 8.2 and 8.3, in the numerical scheme we multiply λ by $1/S_j$ with $S_j = S(x_j^+)$, and in the CFL conditions (3.30), multiply the Courant number α by $S_{\min}/S_{\max}$, where $S_{\min}$ and $S_{\max}$ denote the minimum and the maximum cross-sectional areas of the vessel, respectively.

For Example 8.1, we present the solution at three different times plus a plot of the cumulate density ϕ, while for Examples 8.2 and 8.3 we consider plots of ϕ only. In Example 8.1, we compare the performances of Schemes 4 and 9, while in Examples 8.2 and 8.3, we use Scheme 9 only. We set $\Delta x = 1/512\,$m in all cases, $\lambda = 738.9\,$s/m for Example 8.1, and $\lambda = 184.725\,$s/m for Examples 8.2 and 8.3.

Figure 10 shows the simulated total oil concentration ϕ of Example 8.1 for $t = 1000\,$s, $t = 10000\,$s, and $t = 150000\,$s, with a zoom into a zone where the solution exhibits strong variation. In Figures 11, 12 and 13 we show the numerical solutions of the concentration of each species and the total oil concentration of the Example 8.1 for $t = 1000\,$s, $t = 10000\,$s, and $t = 150000\,$s, respectively, over intervals where the solutions are different from zero. Clearly, the larger species settle first and fill the upper layers of the vessel.
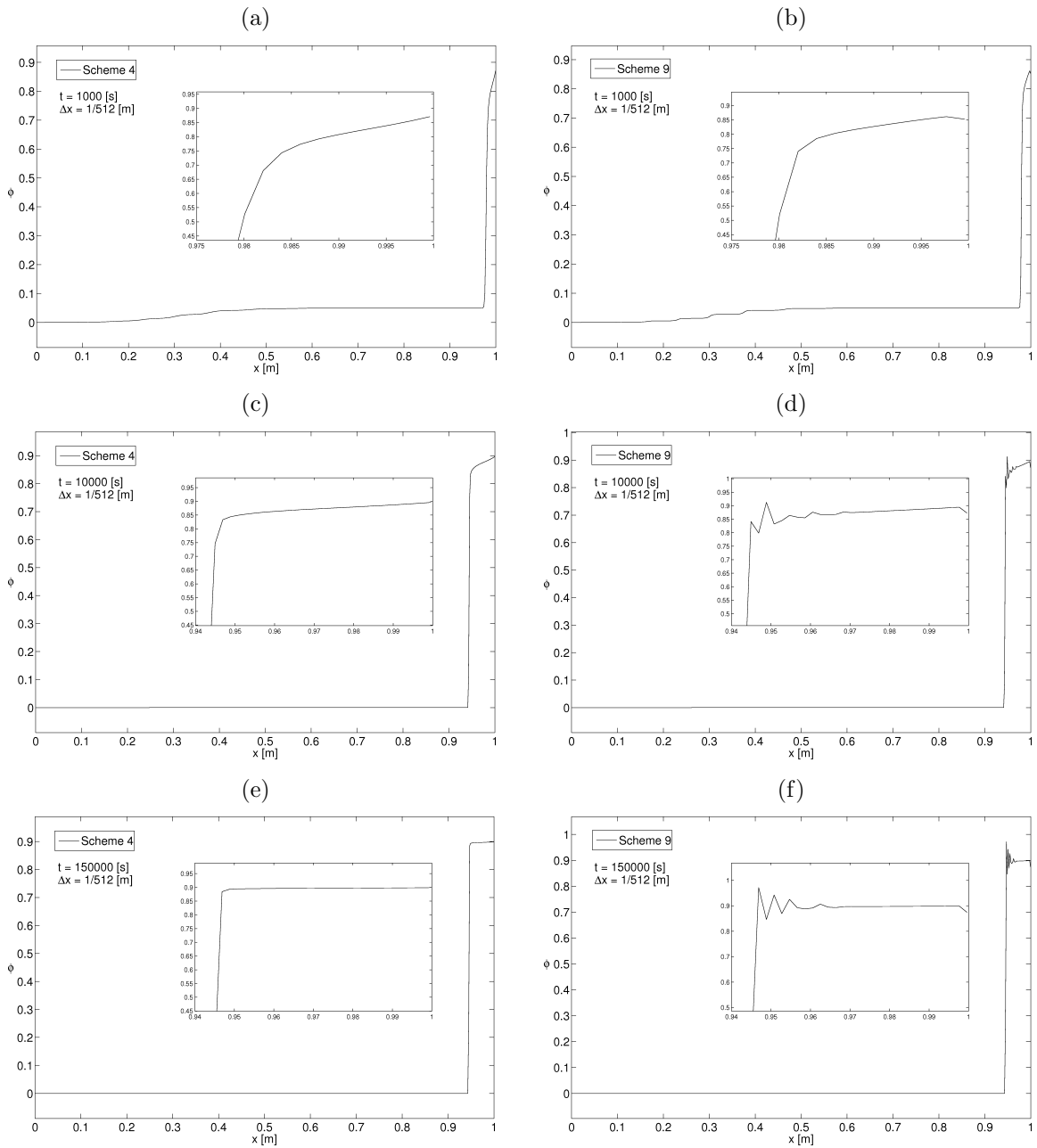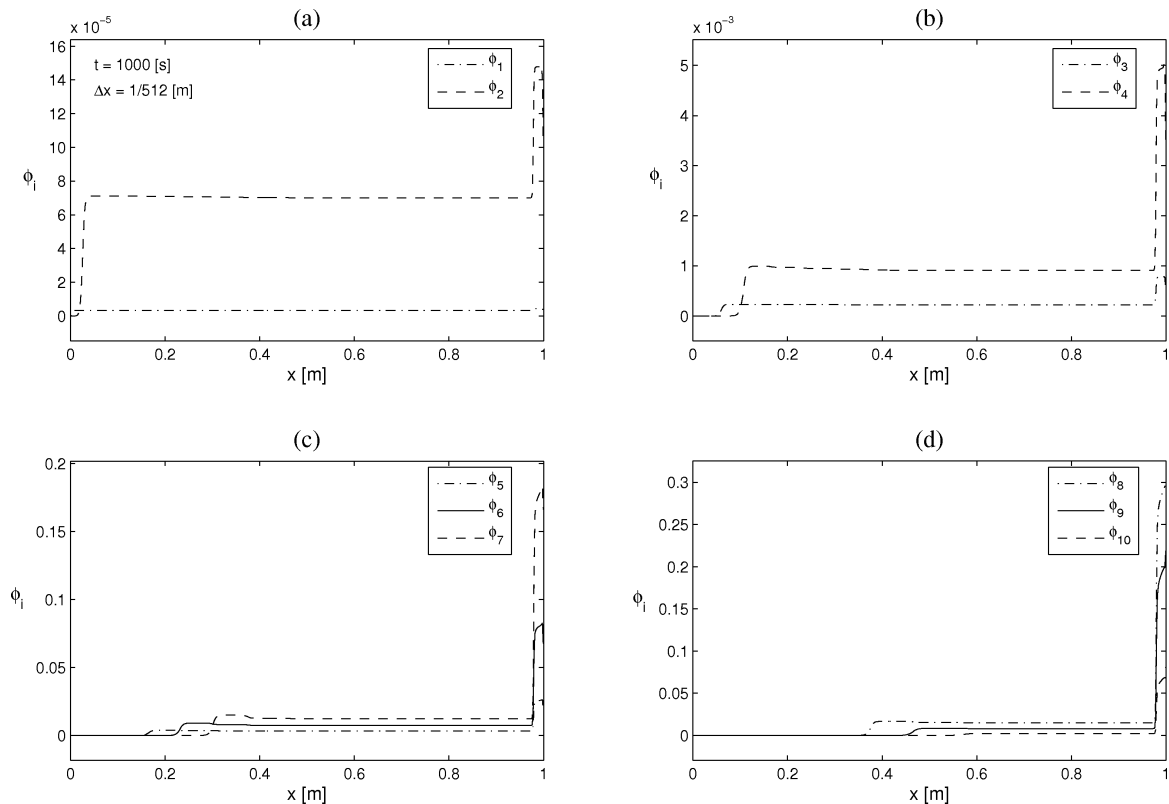
FIGURE 10. Example 8.1 (creaming of a oil-in-water dispersion with $N = 10$ droplet sizes in Vessel 1): simulated total oil concentration with Schemes 4 and 9: (a, b) at $t = 1000\,\mathrm{s}$, (c, d) at $t = 10000\,\mathrm{s}$, and (e, f) at $t = 150000\,\mathrm{s}$.

Figures 14 (a), (c) and (e) show the numerical solutions of the total oil concentration of Example 8.2 (creaming of a oil-in-water dispersion with 10 different droplet sizes in Vessel 2) at three different times, with a zoom in a zone with many changes in the solution, while Figures 14 (b), (d) and (f) display the corresponding results of Example 8.3.

FIGURE 11. Example 8.1 (creaming of an oil-in-water dispersion with $N = 10$ droplet sizes in Vessel 1): concentrations at $t = 1000\,\text{s}$ simulated by Scheme 9.

We notice the effect of the geometry of Vessels 2 and 3 on the concentration profile. In the case of Vessel 2, for $t = 1000\,\text{s}$, the expansion of the area produces an instantaneous decrease of the total concentration at $x = 0.5\,\text{m}$. In the case of Vessel 3, for $t = 1000\,\text{s}$, due to the contraction of the area, the total concentration increases instantaneously just below $x = 0.5\,\text{m}$, decreases strongly in $x = 0.5\,\text{m}$, and then decreases smoothly. Moreover, near steady state, for example at $t = 150000\,\text{s}$, the thickness of the sediment in Vessel 2 is smaller than that in Vessel 3. We see that in general that there is some oscillation in the solution using Scheme 9 at the location of a large jump in ϕ; this does not seem to be present with the first order version of the scheme (Scheme 4). This is left as a problem for future investigation.

REFERENCES

[1] Benzoni-Gavage S, Colombo RM (2003) An n-populations model for traffic flow. Eur J Appl Math 14:587–612
[2] Wong GCK, Wong SC (2002) A multi-class traffic flow model—an extension of LWR model with heterogeneous drivers. Transp Res A 36:827–841
[3] Wong SC, Wong GCK (2002) An analytical shock-fitting algorithm for LWR kinematic wave model embedded with linear speed-density relationship. Transp Res B 36:683–706
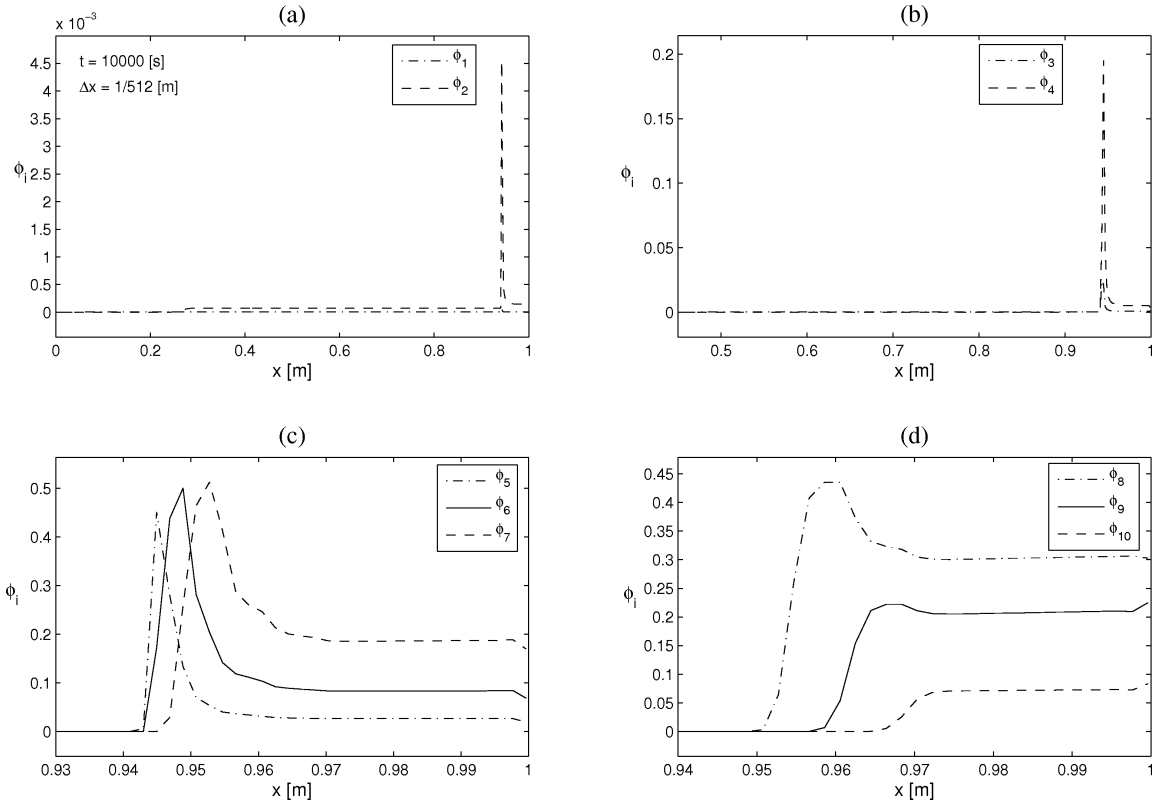
FIGURE 12. Example 8.1 (creaming of a oil-in-water dispersion with $N = 10$ droplet sizes in Vessel 1): concentrations at $t = 10000\,\mathrm{s}$ simulated by Scheme 9.

[4] Zhang M, Shu CW, Wong GCK, Wong SC (2003) A weighted essentially non-oscillatory numerical scheme for a multi-class Lighthill-Whitham-Richards traffic flow model. J Comp Phys 191:639–659

[5] Zhang P, Liu RX, Wong SC, Dai SQ (2006) Hyperbolicity and kinematic waves of a class of multi-population partial differential equations. Eur J Appl Math 17:171–200

[6] Zhang P, Wong SC, Shu CW (2006) A weighted essentially non-oscillatory numerical scheme for a multi-class traffic flow model on an inhomogeneous highway. J Comp Phys 212:739–756

[7] Berres S, Bürger R, Karlsen KH, Tory EM (2003) Strongly degenerate parabolic-hyperbolic systems modeling polydisperse sedimentation with compression. SIAM J Appl Math 64 (2003) 41–80

[8] Bürger R, Karlsen KH, Tory EM, Wendland WL (2002) Model equations and instability regions for the sedimentation of polydisperse suspensions of spheres. ZAMM Z Angew Math Mech 82:699–722

[9] Tory EM, Ford RA, Bargieł M (2003) Simulation of the sedimentation of monodisperse and polydisperse suspensions. In: Wendland WL, Efendiev M (Eds.), Analysis and Simulation of Multifield Problems, Springer-Verlag, Berlin, 343–348

[10] Xue B, Sun Y (2003) Modeling of sedimentation of polydisperse spherical beads with a broad size distribution. Chem Eng Sci 58:1531–1543

[11] Zeidan A, Rohani A, Bassi A, Whiting P (2003) Review and comparison of solids settling velocity models. Reviews in Chemical Engrg 19:473–530

[12] Rosso F, Sona G (2001) Gravity-driven separation of oil-water dispersions. Adv Math Sci Appl 11:127–151

[13] Mochon S (1987) An analysis of the traffic on highways with changing surface conditions. Math Modelling 9:1–11

[14] Bürger R, Karlsen KH (2003) On a diffusively corrected kinematic-wave traffic model with changing road surface conditions. Math Models Meth Appl Sci 13:1767–1799

[15] Bürger R, García A, Karlsen KH, Towers JD (2006) On an extended clarifier-thickener model with singular source and sink terms. Eur J Appl Math 17:257–292

[16] Bürger R, Karlsen KH, Risebro NH, Towers JD (2004) Well-posedness in BV_t and convergence of a difference scheme for continuous sedimentation in ideal clarifier-thickener units. Numer Math 97:25–65
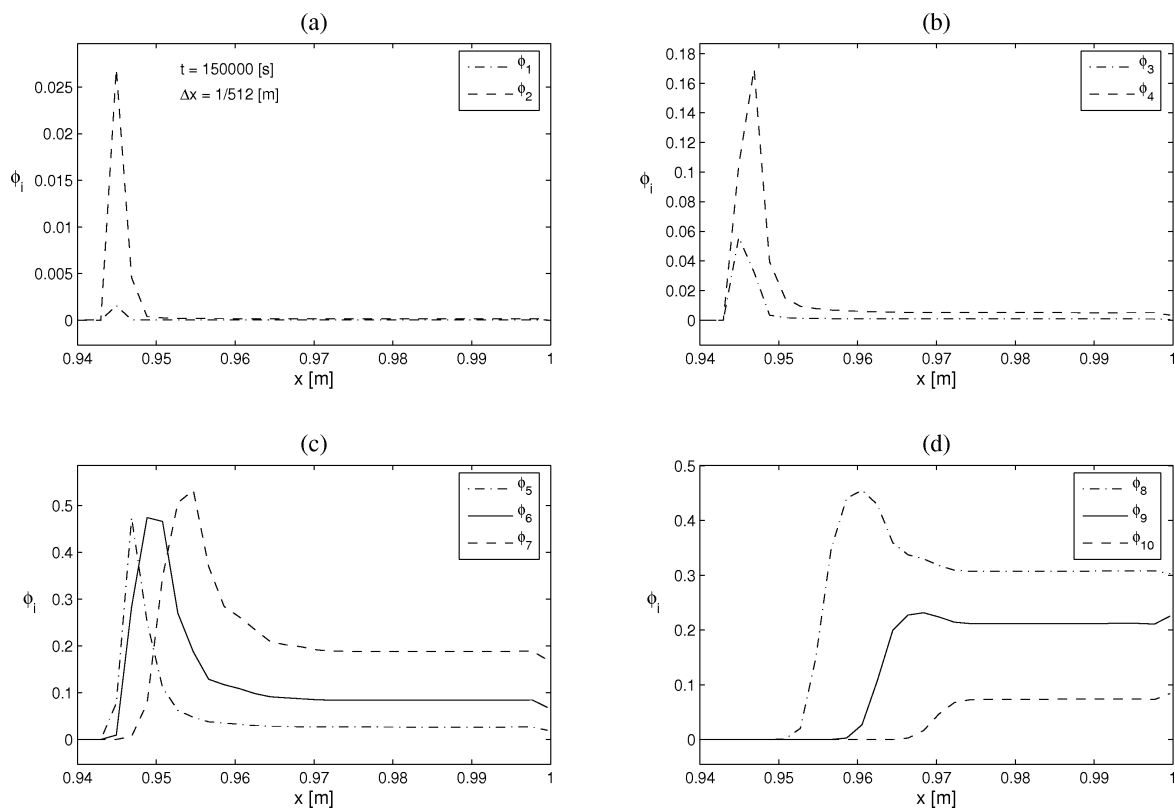
FIGURE 13. Example 8.1 (creaming of a oil-in-water dispersion with $N = 10$ droplet sizes in Vessel 1): concentrations at $t = 150000\,\mathrm{s}$ simulated by Scheme 9.

[17] Lighthill MJ, Whitham GB (1955) On kinematic waves. II. A theory of traffic flow on long crowded roads. Proc Roy Soc London Ser A 229:317–345

[18] Richards PI (1956) Shock waves on the highway. Oper Res 4:42–51

[19] Kynch GJ (1952) A theory of sedimentation. Trans Faraday Soc 48:166–176

[20] Bürger R, Concha F, Fjelde KK, Karlsen KH (2000) Numerical simulation of the settling of polydisperse suspensions of spheres. Powder Technol 113:30–54

[21] Lockett MJ, Bassoon KS (1979) Sedimentation of binary particle mixtures. Powder Technol 24:1–7

[22] Masliyah JH (1979) Hindered settling in a multiple-species particle system. Chem Eng Sci 34:1166–1168

[23] Bürger R, Fjelde KK, Höfler K, Karlsen KH (2001) Central difference solutions of the kinematic model of settling of polydisperse suspensions and three-dimensional particle-scale simulations. J Eng Math 41:167–187

[24] Qian S, Bürger R, Bau HH (2005) Analysis of sedimentation biodetectors. Chem Eng Sci 60:2585–2598

[25] Kurganov A, Tadmor E (2000) New high resolution central schemes for nonlinear conservation laws and convection-diffusion equations. J Comp Phys 160:241–282

[26] Nessyahu H, Tadmor E (1990) Non-oscillatory central differencing for hyperbolic conservation laws. J Comp Phys 87:408–463

[27] Simura R, Ozawa K (2006) Mechanism of crystal redistribution in a sheet-like magma body: Constraints from the Nosappumisaki and other Shoshonite intrusions in the Nemuro prenisula, Northern Japan. J Petrology 47:1809–1851.

[28] Wang X, Miles NJ, Kingman S (2006) Numerical study of centrifugal fluidized bed separation. Minerals Eng 19:1109–1114

[29] Bürger R, Kozakevicius A (2006) Adaptive multiresolution WENO schemes for multi-species kinematic flow models. Preprint 2006-06, Departamento de Ingeniería Matemática, Universidad de Concepción, Chile.

[30] Kružkov SN (1970) First order quasilinear equations in several independent variables. Math USSR Sb 10:217–243

[31] Adimurthi, Veerappa Gowda GD (2002) Conservation law with discontinuous flux. J Math Kyoto Univ 42: 27–70

[32] Audusse E, Perthame B (2005) Uniqueness for a scalar conservation law with discontinuous flux via adapted entropies. Proc Royal Soc Edinburgh Sect A 135:253–265
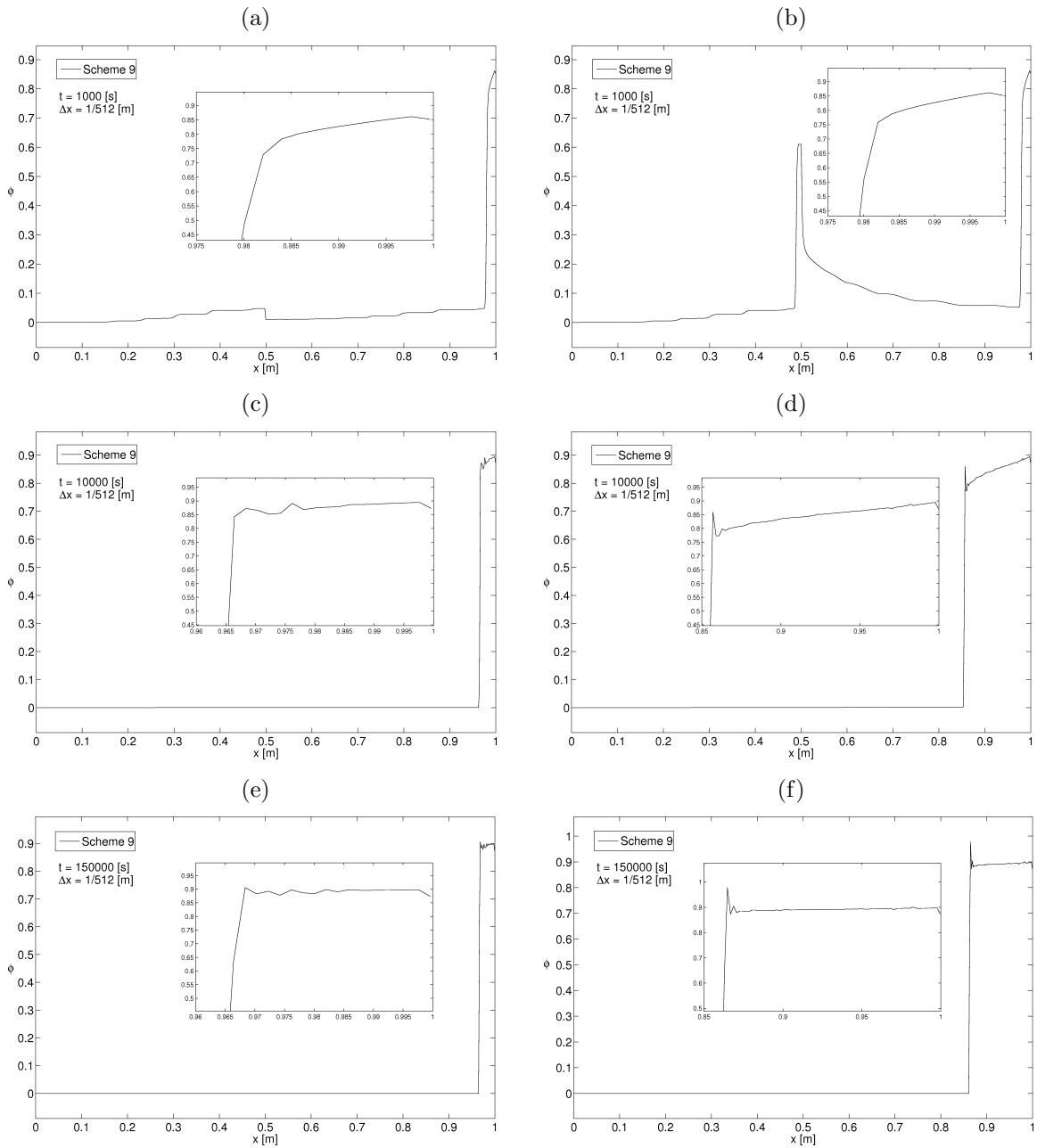
FIGURE 14. Examples 8.2 and 8.3 (creaming of a oil-in-water dispersion with $N = 10$ droplet sizes in Vessels 2 (a, c, e) and 3 (b, d, f)): total oil concentration simulated by Scheme 9 at (a, b) $t = 1000\,\text{s}$, (c, d) $t = 10000\,\text{s}$ and (e, f) $t = 150000\,\text{s}$.

[33] Bachmann F, Vovelle J (2006) Existence and uniqueness of entropy solution of scalar conservation laws with a flux function involving discontinuous coefficients. Comm Partial Diff Eqns 31:371–395

[34] Gimse T (1993) Conservation laws with discontinuous flux functions. SIAM J Math Anal 24:279–289

[35] Gimse T, Risebro NH (1992) Solution of the Cauchy problem for a conservation law with a discontinuous flux function. SIAM J Math Anal 23:635–648

[36] Karlsen KH, Klingenberg C, Risebro NH (2003) A relaxation scheme for conservation laws with a discontinuous coefficient. Math Comp 73:1235–1259

[37] Karlsen KH, Risebro NH, Towers JD (2002) Upwind difference approximations for degenerate parabolic convection-diffusion equations with a discontinuous coefficient. IMA J Numer Anal 22:623–664

[38] Karlsen KH, Risebro NH, Towers JD (2003) L^1 stability for entropy solutions of nonlinear degenerate parabolic convection-diffusion equations with discontinuous coefficients. Skr K Nor Vid Selsk, 49 pp

[39] Karlsen KH, Towers, JD (2004) Convergence of the Lax-Friedrichs scheme and stability for conservation laws with a discontinuous space-time dependent flux. Chin Ann Math 25B:287–318

[40] Klausen RA, Risebro NH (1999) Stability of conservation laws with discontinuous coefficients. J Diff Eqns 157:41–60

[41] Klingenberg C, Risebro NH (1995) Convex conservation laws with discontinuous coefficients. Comm Partial Diff Eqns 20:1959–1990

[42] Mishra S (2005) Convergence of upwind finite difference schemes for a scalar conservation law with indefinite discontinuities in the flux function. SIAM J Numer Anal 43:559–577

[43] Seguin N, Vovelle J (2003) Analysis and approximation of a scalar conservation law with a flux function with discontinuous coefficients. Math Models Meth Appl Sci 13:221–257

[44] Towers JD (2000) Convergence of a difference scheme for conservation laws with a discontinuous flux. SIAM J Numer Anal 38:681–698

[45] Towers JD (2001) A difference scheme for conservation laws with a discontinuous flux: The nonconvex case. SIAM J Numer Anal 39:1197–1218

[46] Bürger R, Karlsen KH, Mishra S, Towers JD (2005) On conservation laws with discontinuous flux. In: Wang Y, Hutter K (Eds.), Trends in Applications of Mathematics to Mechanics, Shaker Verlag, Aachen, 75–84

[47] Bürger R, Karlsen KH, Towers JD (2005) A mathematical model of continuous sedimentation of flocculated suspensions in clarifier-thickener units. SIAM J Appl Math 65:882–940

[48] Diehl S (2001) Operating charts for continuous sedimentation I: Control of steady states. J Eng Math 41:117–144

[49] Diehl S (2005) Operating charts for continuous sedimentation II: Step responses. J Eng Math 53:139–185

[50] Diehl S (2006) Operating charts for continuous sedimentation III: Control of step inputs. J Eng Math 54:225–259

[51] Diehl S (2006) Operating charts for continuous sedimentation IV. In preparation.

[52] Bürger R, Karlsen KH, Klingenberg C, Risebro, NH (2003) A front tracking approach to a model of continuous sedimentation in ideal clarifier-thickener units. Nonlin Anal Real World Appl 4:457–481

[53] Berres S, Bürger R, Karlsen KH (2004) Central schemes and systems of conservation laws with discontinuous coefficients modeling gravity separation of polydisperse suspensions. J Comp Appl Math 164-165:53–80

[54] Bürger R, García A, Karlsen KH, Towers JD (2006) A kinematic model of continuous separation and classification of polydisperse suspensions. Preprint 2006-18, Departamento de Ingeniería Matemática, Universidad de Concepción, Chile.

[55] Schneider W, Anestis G, Schaflinger U (1985) Sediment composition due to settling of particles of different sizes. Int J Multiphase Flow 11:419–423

[56] Hartland S, Jeelani SAK (1987) Choice of model for predicting the dispersion height in liquid/liquid gravity settlers from batch settling data. Chem Eng Sci 42:1927–1938

[57] Hartland S, Jeelani SAK (1988) Prediction of sedimentation and coalescence profiles in a decaying batch dispersion. Chem Eng Sci 43:2421–2429

[58] Jeelani SAK, Hartland S (1988) Dynamic response of gravity settlers to changes in dispersion throughput. AIChE J 34:335–340

[59] Jeelani SAK, Hartland S (1993) The continuous separation of liquid/liquid dispersions. Chem Eng Sci 48:239–254

[60] Jeelani SAK, Pandit A, Hartland S (1990) Factors affecting the decay of batch liquid-liquid dispersions. Canad J Chem Eng 68:924–931

[61] Nadiv C, Semiat R (1995) Batch settling of liquid-liquid dispersion. Ind Eng Chem Res 34:2427–2435

[62] Frising T, Noïk C, Dalmazzone C (2006) The liquid/liquid sedimentation process: From droplet coalescence to technologically enhanced water/oil emulsion gravity separators: A review. J Disp Sci Technol 27:1035–1057

[63] Panoussopoulos K (1998) Separation of Crude Oil-Water Emulsions: Experimental Techniques and Models. Dissertation, ETH Zürich, Switzerland.

[64] Crandall MG, Majda A (1980) Monotone difference approximations for scalar conservation laws. Math Comp 34:1–21

[65] Harten A (1983) High Resolution schemes for hyperbolic conservation laws. J Comp Phys 49:357–393

[66] Tadmor E (1984) Numerical viscosity and the entropy condition for conservative difference schemes. Math Comp 43:369–381

[67] Le Veque RJ (1992) Numerical Methods for Conservation Laws, Birkhauser Verlag, Basel, Switzerland.

[68] Gottlieb S, Shu CW, Tadmor E (2001) Strong stability preserving high-order time discretization methods. SIAM Review 43:89-112

[69] Osher S (1985) Convergence of generalized MUSCL schemes. SIAM J Numer Anal 22:947–961

[70] Shannon PT, Stroupe E, Tory EM (1963) Batch and continuous thickening. Ind Eng Chem Fund 2:203–211

[71] Das SK, Biswas MN (2003) Separation of oil-water mixture in tank. Chem Eng Comm 190:116–127